Chapter 3
Development and Operation of Underwater Robot for Autonomous Tracking and Monitoring of Subsea Plumes After Oil Spill and Gas Leak from Seabed and Analyses of Measured Data

Mahdi Choyekh, Naomi Kato, Yasuaki Yamaguchi, Ryan Dewantara, Hajime Chiba, Hidetaka Senga, Muneo Yoshie, Toshinari Tanaka, Eiichi Kobayashi, and Timothy Short

Abstract Oil spills produced by accidents from oil tankers and blowouts of oil and gas from offshore platforms cause tremendous damage to the environment as well as to marine and human life. To prevent oil and gas that are accidentally released from deep water from spreading and causing further damage to the environment over time, early detection and monitoring systems can be deployed to the area where underwater releases of the oil and gas first occurred. Monitoring systems can provide a rapid inspection of the area by detecting chemical substances and

M. Choyekh (✉) • N. Kato • Y. Yamaguchi • R. Dewantara • H. Senga
Naval Architecture and Ocean Engineering, Osaka University, Yamadaoka 2-1, Suita, Osaka 565-0871, Japan
e-mail: mahdi.choyekh@gmail.com; kato@naoe.eng.osaka-u.ac.jp; yamaguchi_yasuaki@naoe.eng.osaka-u.ac.jp; ryan.putra.dewantara@gmail.com; senga@naoe.eng.osaka-u.ac.jp

H. Chiba
Department of Merchant Marine, Toyama National College of Technology, 1-2 Ebieneriya, Imizu, Toyama 933-0293, Japan
e-mail: chiba@nc-toyama.ac.jp

M. Yoshie • T. Tanaka
New technology Development Field, Port and Airport Research Institute, 3-1-1 Nagase, Yokosuka, Kanagawa 239-0826, Japan
e-mail: yoshie@pari.go.jp; tanaka_t@pari.go.jp

E. Kobayashi
Graduate School of Maritime Sciences, Kobe University, 5-1-1 Fukaeminami, Higashinada-ku, Kobe, Hyogo 658-0022, Japan
e-mail: kobayasi@maritime.kobe-u.ac.jp

T. Short
Marine and Space Sensing, SRI International, 450 Eighth Avenue SE, St. Petersburg, FL 33701, USA
e-mail: timothy.short@sri.com

N. Kato (ed.), *Applications to Marine Disaster Prevention*,
DOI 10.1007/978-4-431-55991-7_3

collecting oceanographic data necessary for enhancing the accuracy of simulation of behavior of oil and gas. An autonomous underwater vehicle (AUV) called the spilled oil and gas tracking autonomous buoy system (SOTAB-I) has been developed to perform on-site measurements of oceanographic data as well as dissolved chemical substances using underwater mass spectrometry. In this chapter, the outlines of SOTAB-I and a description of its hardware and software are presented. The operating modes and guidance and control of the robot are detailed. The experimental results obtained during the early deployments of SOTAB-I in the shallow water of the Gulf of Mexico in the USA demonstrated the ability of SOTAB-I to collect substances' dissolutions in seawater such as hydrocarbons. Deepwater experiments were conducted in Toyama Bay in Japan and enabled demonstration of the ability of SOTAB-I to establish the vertical water column distribution of oceanographic data, such as temperature, salinity, and density. In addition, a high-resolution profile of water currents was obtainable.

Keywords AUV • Survey • Chemical substances • Oceanographic data

3.1 Introduction

The world economy depends to a large extent on the use of energy. To meet the increasing need for energy, both in industry and daily life, petroleum activities, such as drilling and shipping, are on the rise. Thus, additional attention is required to avoid accidents that can happen due to such activities. Oil spills and blowouts of oil and gas from the seabed cause serious damage to the environment as well as to the economy, not to mention the damage to marine and human life. For the case in which methane gas is blown out from a seabed, it is partly dissolved in seawater and then partly consumed by methanotrophs (Kessler et al. 2011), which leads to the creation of local hypoxia zones caused by oxygen depletion (Shaffer et al. 2009). The rest of the gas is released to the atmosphere, contributing to global warming, as methane is a highly potent greenhouse gas (Solomon et al. 2009). Recently, several oil spill accidents have happened. Deepwater Horizon in the Gulf of Mexico in 2010 and the Elgin gas platform in the North Sea in 2012 are examples of these accidents. To prevent oil and gas spills from spreading and causing further damage to the environment over time, early detection and monitoring systems can be deployed around the offshore oil and gas production system. In addition, oceanographic data should be collected to comprehend the environmental changes around the accident. Based on the collected information, oil and gas drifting simulations must be performed to predict where the spilled oil will wash ashore and to adequately deploy oil recovery machines before this occurs.

A wide variety of methods that deal with underwater oil spills exists, and each presents strengths and weaknesses according to the circumstances and the purposes for which it is deployed. For substances' dissolution measurement, among the most commonly used techniques is the extraction of discrete samples for subsequent analyses (Joye et al. 2011). However, this method has limited temporal

and spatial resolution. Additionally, it requires much effort and is time consuming. Furthermore, a risk is that the characteristics of the original collected samples could change during the collecting and handling processes. Other techniques are utilized to track a particular substance, such as oxygen, methane, or carbon dioxide. These methods can provide continuous information regarding the dissolution of substances, but only for a particular and limited variety of substances. The spilled oil and gas tracking autonomous buoy system (SOTAB-I) integrates an underwater mass spectrometer (UMS) that overcomes the previously mentioned weaknesses. The UMS enables real-time on-site measurements. It is distinguished by its good flexibility and sensitivity as well as its high reliability. It can detect multiple substances' dissolutions simultaneously (Short et al. 2006).

The challenge in water surveying is not only to detect oil and substances dissolved in seawater but also to obtain other related oceanographic data, as many research programs have demonstrated that temperature (Servio and Englezons 2002), pressure (Handa 1990), and salinity (Yang and Xu 2007) are critical factors that considerably affect the formation and dissociation of gas hydrate. In addition, measurement of underwater currents is important for detecting and tracking dissolved gases and for predicting the evolution of the blowout gas in simulation models. Few existing compact systems are able to conduct a complete survey that can measure salinity, temperature, and depth as well as underwater currents and dissolved gases simultaneously. In Deep Spill experiments in Norway, for example, substances' dissolutions were collected using a rosette with sampling flasks towed from a ship. Underwater current data were collected from two separate acoustic Doppler current profiler (ADCP) devices, one on board a second ship and the other connected to an acoustic transmitter and moored on the seabed (Johansen et al. 2003). Using such a technique is helpful to obtain a full survey of the area. However, it requires good synchronization while operating because sensors are mounted in different places. In addition, it requires further resources for deployment, which increases the cost of the survey. The SOTAB-I combines necessary sensors for a full and complete real-time and on-site survey by integrating a UMS, an acoustic Doppler current profiler (ADCP), a conductivity-temperature-depth sensor (CTD), and a camera.

Another challenge related to underwater surveying efforts is the range of the survey. For example, for water profiling, few systems that can provide a deepwater profile exist. Existing acoustic water profiling sensors based on ADCP can barely perform measurements of water current distribution beyond the limit of 1000 m depth from the sea surface. Furthermore, in most ADCP devices, resolution of the water layer decreases when higher ranges are applied. Some investigations could lead to a longer range by using multiple ADCP devices. For instance, a solution that implements a dual-meter system based on a surface- and a bottom-mounted ADCP was suggested (Vogel et al. 2001). The system could measure the water currents' profile up to 1200 m. However, the system lacks the flexibility needed for prompt intervention missions. The SOTAB-I has the capability to perform a high-resolution survey with extended range from sea surface up to a water depth of 2000 m.

Due to their compactness, the use of AUVs for full-water surveying is being adopted increasingly (Jakuba et al. 2011; Harvey et al. 2012). Among the existing

types of underwater robots used to autonomously monitor marine environments in 3D space from sea surface to seabed over the long term is the Argo Float (Roemmich et al. 2009) that floats vertically and repeats descending and ascending in the vertical direction by using a buoyancy control device. However, it does not have a function of active movement in the horizontal direction. Another method is the underwater glider (Eriksen et al. 2001), which has a streamlined body with fixed wings. It can descend and ascend also by using a buoyancy control device, while it moves in the horizontal plane like a glider for long distance. However, the ratio of vertical movement distance to horizontal movement distance is small. SOTAB-I was designed to move not only in the vertical direction by a buoyancy control device but also in the horizontal direction by two pairs of rotational fins.

The development of a new type of AUV requires an evaluation process from two aspects. One is the guidance and control of the vehicle and the other is the data sampling. In the first part of this chapter, descriptions of the underwater robot SOTAB-I and its hardware and software are presented. In the second part, the maneuverability of the SOTAB-I is described. The third part shows the survey results obtained in shallow water in the Gulf of Mexico in the USA and in deep water in Toyama Bay in Japan.

3.2 SOTAB-I Overview

3.2.1 Outlines of SOTAB-I

The SOTAB-I is 2.5 m long and weighs 325 kg. It can be submerged in water as deep as 2000 m. It is able to descend and ascend by adjusting its buoyancy using a buoyancy control device while changing its orientation through two pairs of movable wings. The SOTAB-I can also move in horizontal and vertical directions using two pairs of horizontal and vertical thrusters. A visual overview of SOTAB-I is illustrated in Fig. 3.1, and its main characteristics are summarized in Table 3.1. The arrangement of devices and sensors installed on SOTAB-I is shown in Fig. 3.2.

When the robot floats on the sea surface, a wireless local area network (WLAN) and an iridium satellite communication transceiver module are used for data transmission. When the robot is underwater, the user on the mother ship and the SOTAB-I can communicate through the acoustic modem.

The robot tracking on the sea surface is ensured by a global positioning system (GPS) receiver that serves to determine the robot's absolute position. In the case where the robot is submerged, tracking is ensured by the ultrashort baseline (USBL) system. The vertical position of the robot in the water column is given by depth data from the CTD sensor. When the robot is within the bottom tracking altitude from the seabed, the Doppler velocity logger (DVL) is able to measure robot's velocities. The robot motion and orientation are given by the compass and the inertial measurement unit (IMU). An ADCP is employed to measure the magnitude and orientation of water current layers. SOTAB-I is also fitted with a UMS to

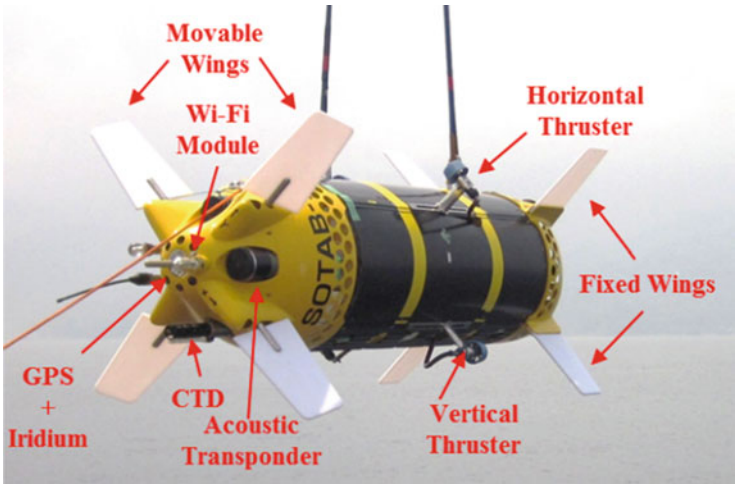

Fig. 3.1 SOTAB-I robot

Table 3.1 Principal particulars of SOTAB-I

Total length [mm]		2503
Diameter [mm]		667
Weight in air [kg]		311.7
Weight in water [kg]		±3.8
Movable wing	Chord [mm]	200
	Span [mm]	400
Fixed wing	Chord [mm]	200
	Span [mm]	400

determine the characteristics and physical properties of the dissolved gas and oil. To obtain a visual representation of blowouts of plumes of gas on the seabed, the robot is equipped with a camera.

3.2.2 Hardware Description

SOTAB-I devices can be classified based on their function, as shown in Fig. 3.3. Following are further details about SOTAB-I hardware.

3.2.2.1 Power Supply

SOTAB-I is powered by 32 packs of lithium-ion batteries divided into pairs and mounted in a serial arrangement. The 16 pairs are then mounted in parallel, which gives a voltage of 28.8 V because every single pack voltage is 14.4 V.

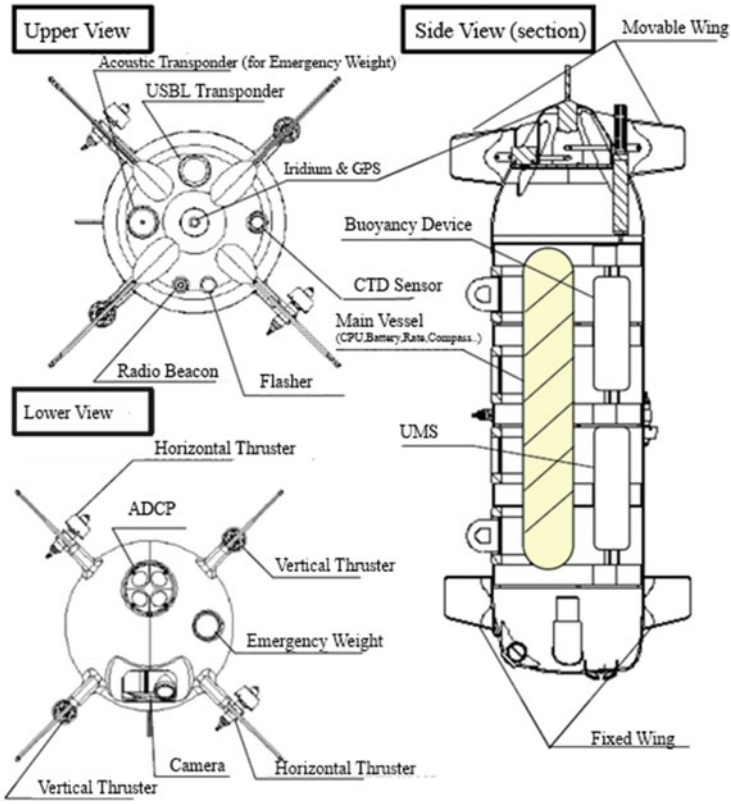

Fig. 3.2 Arrangement of devices and sensors installed on SOTAB-I

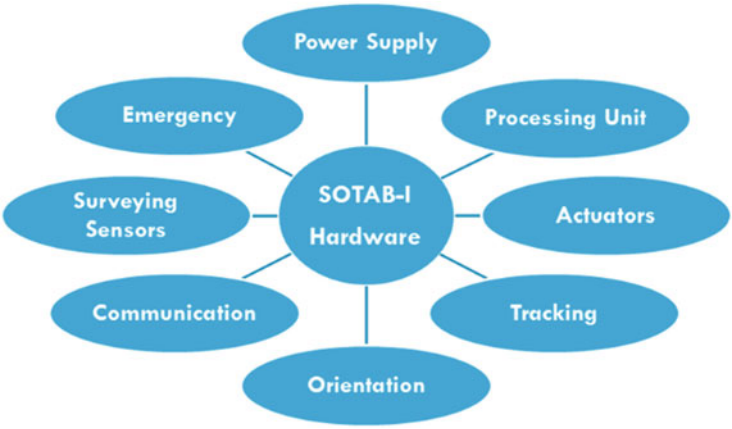

Fig. 3.3 Hardware classification

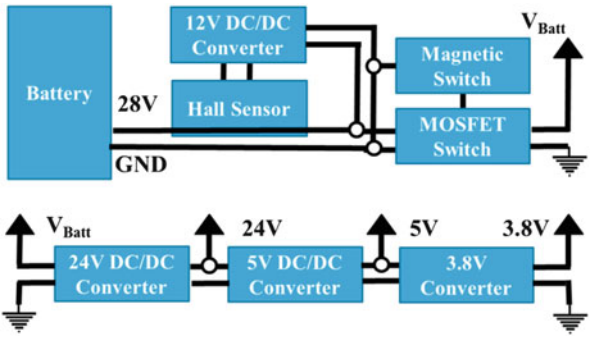

Fig. 3.4 Power supply conversion

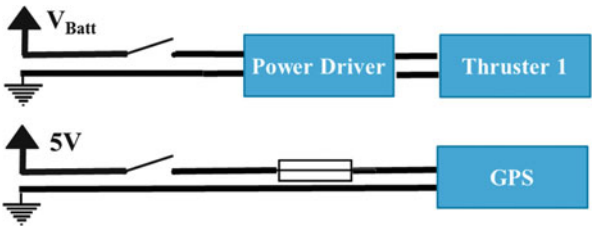

Fig. 3.5 Power supply of actuators and sensors

The total capacity of the batteries is equal to 4608 W•h. Table 3.11 presents the characteristics of the batteries used. As shown in Fig. 3.4, the power is activated via an external magnetic switch that controls the gate of the power MOSFET (metal-oxide-semiconductor field-effect transistor), used here as a power switch. DC/DC converters are employed to convert the battery voltage output to the different levels of power supply required for the operation of the internal devices. A hall sensor is used to measure the current. Two power switch control boards serve to control the power supply of internal devices. They also include necessary fuses used for protection against surcharges. Power activation of each sensor/actuator is controlled by the processing unit board I/O port. Control boards and power boards are optically separated. Figure 3.5 shows a typical electronic circuit used for powering the GPS sensor. The same concept is used for all other sensors, with the only difference in the input voltage. An example of a circuit used to power the thruster 1 is also shown in Fig. 3.5. Similarly, all actuators such as thrusters, wings, and buoyancy device have the same power supplying concept. Table 3.2 shows the power consumption of sensors installed on SOTAB-I.

3.2.2.2 Processing and Control Unit

The processing unit of the SOTAB-I is made up of two processors. The volatile memory capacity is 1 GB. The characteristics of the processing unit are detailed in Table 3.12. The board has an Ethernet port connected to a Wi-Fi router that serves to connect to a remote computer through a wireless local area network (LAN). The

Table 3.2 Power consumption of sensors

Sensor	Power consumption
CTD	3.4 W (typical)
UMS	60–80 W
DVL	3 W (typical)
USBL	100 W (during transmission)
Iridium	1 W
GPS	0.4 W (typical)
IMU	0.22 W (maximum)
LAN	2.3 W (maximum)
CPU	16.27 W (typical), 25.3 W (maximum)

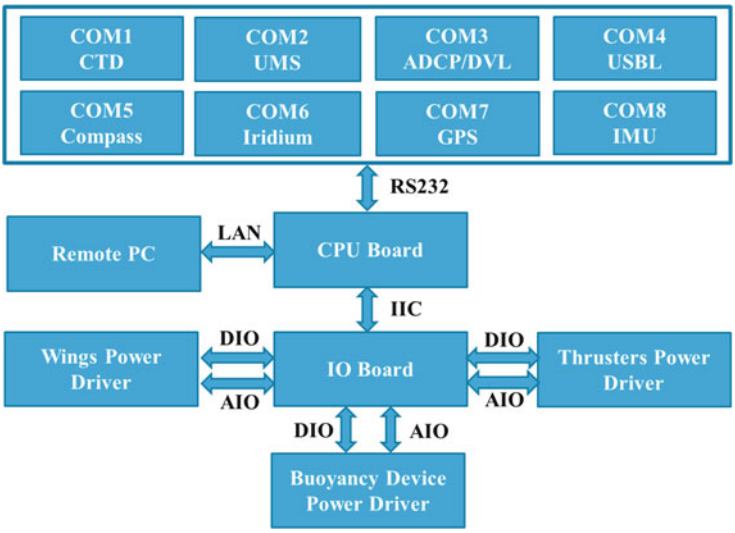

Fig. 3.6 Computer communication interfaces

processing unit is also fitted with several interfaces such as USB, RS-232, and inter-integrated circuit (I^2C). Three of the USB ports are used to connect external flash memories. The SOTAB-I computer is composed of three storage drives. The C drive is used for the operating system, the E drive for the programs' setup files, and the D drive for logging and program storage.

All sensors are directly interfaced through their respective RS-232 serial ports. Internally, the CPU board connects to an input/output board (IO board) through the inter-integrated circuit (I^2C) serial interface. The IO board is composed of circuits that are able to interface with 32 digital input outputs (DIO), 8 analog outputs using digital-to-analog converters (DAC), and 8 analog inputs (AI) using analog-to-digital converters (ADC). The IO board ensures isolation between the CPU board and the power drivers. CPU board interfaces are summarized in Fig. 3.6.

3.2.2.3 Actuators

Buoyancy Device

In the buoyancy control device, an oil hydraulic pump injects and extracts oil between the external oil bladder and the internal oil reservoir. A motor valve serves to automate opening and closing cycles, and a brake is used to lock the pump (Fig. 3.7). The flow rate during the injection of oil into the bladder at the external pressure of 20 MPa is 243 mL/min, and during the extraction of oil from the bladder at the same external pressure condition, it is 349 mL/min. In total, six digital inputs are employed to control the buoyancy device. A digital input serves to control the power supply relay. One input is used to open the valve and another to close it. To control the motor pump actuator, one input is used to run/disable it and another one specifies the rotation direction. One more serves to activate/deactivate the brake. The feedback is provided by two digital outputs that report the valve position and one analog output that provides the oil level.

Figure 3.8 depicts the relationship between the pressure in the reservoir and the volume of the oil in the reservoir. The "pressure in the reservoir" is the pressure applied by the hydraulic pump to the oil reservoir cylinder. The maximum allowable drain pressure of the pump is 0.03 MPa. The oil reservoir is fitted with a linear potentiometer whose analog output voltage is an image of the piston displacement under the pump drain pressure. The voltage is proportional to the oil volume of the reservoir, which leads to the variation of robot buoyancy, as shown in Table 3.3. When the oil room is full, the output voltage is 0.3892 V. When the oil room is empty, the output voltage is 1.6208 V. Because the reservoir has a cylindrical shape and the surface of the base is constant, the output voltage of the potentiometer can be used to determine the volume of the oil in the reservoir, which explains the linear volume/output voltage relationship. The mass change can be obtained after

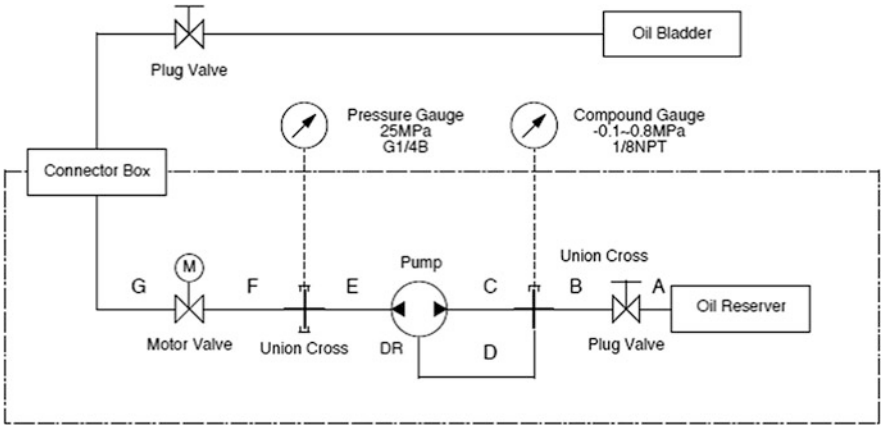

Fig. 3.7 Buoyancy device

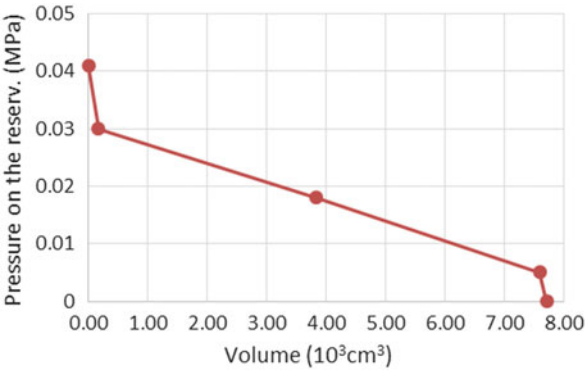

Fig. 3.8 Relationship between the pressure and the volume in the oil reservoir

Table 3.3 Variation of robot buoyancy against voltage on motor

Mass change (seawater) (g)	Volume change (cm^3)	Potentiometer output voltage (V)	Pressure (MPa)
7,884.8	7,700.0	1.621	0
7,746.6	7,565.0	1.599	0
7,763.2	7,581.2	1.602	0.005
3,925.7	3,833.7	1.012	0.018
171.8	167.8	0.443	0.030
0	0	0.389	0.041

multiplying the volume change with the density of seawater, which is typically equal to 1024 kg/m^3.

Wings

The robot is equipped with two pairs of rotational wings situated at the top side of the robot and four fixed wings attached at the bottom side. Each pair of movable wings is controlled around a rotational axis with the same direction and angle by a servomotor, and the rotational axis of one pair of movable wings is perpendicular to that of the other. DC motor drives connected to a gearhead with a 53:1 ratio enable each pair of wings to move from −90 to 90°. A rotational potentiometer with a resolution better than 0.1° provides information about the current orientation of the wings. A separate microcontroller control board integrating a proportional-integral-derivative (PID) controller program is used to control the wings through a serial port. The typical power consumption of the wing drive is 7 W.

Thrusters

Thrusters are controlled by an analog input varying from 0 to ±5 V. A relay is used for turning the power on and off. A tachometer measures the rotational speed and converts it to an analog output. Each thruster has a maximum thrust force equal to 35.28 N forward and 26.46 N backward. Table 3.12 gives more details about thruster specifications.

3.2.2.4 Tracking

The robot absolute position is needed for several purposes, notably for robot guidance and water survey. Robot control relies on underwater position to determine the direction and distance in which the robot should go. The concentration of oil substances will be assigned to their absolute position. Then it is possible to know the distribution of oil in the area and use that to develop a strategy to track the oil slick or find the blowout gas source. SOTAB-I is fitted with a GPS receiver that can output the robot's absolute position when it is on the sea surface. DGPS accuracy is better than 3 m with 95 % confidence. The characteristics of the GPS receiver are described in Table 3.14. The high-frequency waves of the global positioning system (GPS) have very low penetrability into water. Instead, acoustic-based positioning systems (APS) are used widely for underwater tracking. Several APS techniques can be used (Vickery 1998). SOTAB-I integrates an ultrashort baseline (USBL) system for underwater positioning. It has the advantage of being very easy to deploy because it only requires a single transceiver on the ship side and one transponder installed on the robot side. In addition, USBL systems have an acceptable range and accuracy. The USBL system deployed with the SOTAB-I can track up to eight targets at a range of up to 5000 m with ship noise. Its accuracy is equal to 0.15° for the bearing angle accuracy and 0.3 m for the slant range. On board the ship, a GPS pole is deployed with a vertical reference unit (VRU) system to determine the absolute position of the ship in addition to the tilting of the acoustic transceiver. The GPS compass has a DGPS horizontal accuracy better than 0.6 m with 95 % confidence. Heading accuracy is better than 0.15° rms. Further details about the GPS compass are described in Table 3.15. The relative underwater position of SOTAB-I to the mother ship is combined with the ship absolute position to determine the absolute position of the robot in the Earth-fixed coordinates. USBL determines the relative position by calculating the range and the angle between the transceiver and the transponder. At first, an acoustic pulse is transmitted by the transceiver. When the robot's transponder detects the pulse, the transponder replies by sending another pulse. The time difference between the transmission of the transceiver pulse and the arrival of the transponder pulse is converted to range, while the phase difference within the transceiver's transducer array determines the angle.

3.2.2.5 Orientation

SOTAB-I is fitted with a tilt-compensated compass module that provides attitude information. The accuracy of the compass module is 0.3 °rms for the heading angle and 0.2 °rms for the tilting angles. The maximum sampling frequency is 20 Hz, and its typical power consumption at that rate is 0.1 W. The module is accompanied with hard and soft iron calibration algorithms that contribute to the improvement of the reliability and consistency of heading measurement. Detailed features of the IMU sensor are detailed in Table 3.20.

SOTAB-I is also equipped with an inertial measurement unit (IMU) and attitude heading reference system (AHRS) that combine three-axis accelerometers, three-axis gyros, three-axis magnetic sensors, a barometric pressure sensor, and a 32-bit built-in microcontroller. The IMU microcontroller runs a quaternion-based extended Kalman filter (EKF), which provides estimates of the attitude of the sensor as well as the real-time gyro biases. It can output acceleration, angular rate, and magnetic measurements along the body coordinate frame as well as in the north–east–down (NED) coordinate frame. The device can also measure the temperature and the barometric pressure. The sensor has already been subject to a factory calibration. Additionally, it provides the user with the ability to apply a separate user calibration to remove additional bias, scale factor, and axis misalignments. The sensor includes a separate EKF that provides real-time estimation of the local magnetic hard and soft iron distortions. The maximum power consumption of the module is 0.22 W. Data measurement update rate, including Kalman filter data processing, can go as high as 300 Hz. The communication with the IMU sensor is performed through an RS-232 serial port, but it is also possible using the SPI interface. The system was configured to output binary message data, which contains the maximum amount of information.

3.2.2.6 Communication

The communication between the SOTAB-I and the mother ship depends on the distance between them and whether the robot is on the sea surface or underwater (Fig. 3.9). When the SOTAB-I is on the sea surface and within a 200 m range of the mother ship, it is possible to remotely connect to the robot computer and take full control of the robot. The UDP port is used to exchange data, such as the state of the joystick control button, between the ship GUI and the robot GUI. SOTAB-I is also fitted with an Iridium satellite communication transceiver module. It has global coverage and can send and receive messages within 6–22 s. Transmission speed is up to 340 bytes per message, and reception speed is up to 270 bytes per message. When the robot is underwater, real-time communication with the ship using radio waves becomes impossible, and acoustic communication is used instead. In the current configuration, the acoustic communication speed is equal to 1320 bytes per 8 s for uplink and 80 bytes per 8 s for downlink. To be able to establish acoustic

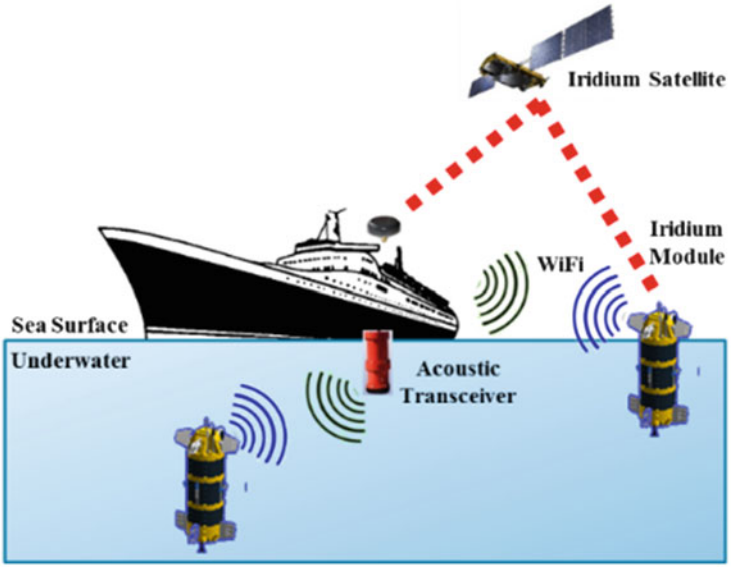

Fig. 3.9 Communication

communication, it is important that the robot be within the operating beam width of the transceiver, which is equal to 120°.

3.2.2.7 Surveying Sensors

CTD

The CTD sensor can measure the temperature, conductivity, and pressure of seawater. Based on those measurements, it is possible to calculate additional oceanographic data such as salinity and density as well as sound speed. The vertical position of the robot in the water column can also be obtained based on the pressure value. The CTD sensor employed has a sampling frequency up to 16 Hz, enabling a very high spatial resolution. It has a high accuracy and a typical power consumption of 3.4 W. A serial RS-232 communication port interfaces with the sensor. The characteristics of the sensor are described in Table 3.16.

ADCP/DVL

An ADCP/DVL device was used for water profiling and bottom tracking. It integrates heading and attitude sensors that are necessary for coordinate transformation. The accuracy is within $\pm 2°$ for the compass and $\pm 0.5°$ for the attitude.

An integrated thermistor measures water temperature and improves the accuracy of calculation of sound speed as well as enhances the accuracy of the acoustic measurements. The device is mounted looking downward at the bottom of the robot, as shown in Fig. 3.2. The device has four piston transducers with standard acoustic frequency equal to 1228.8 kHz, which enables high-resolution measurements of water currents up to 13 m range at 0.5 m layer resolution. The number of layers is selectable, and the layer thickness can be customized from 0.25 to 5 m. When the robot is within the bottom tracking altitude from the seabed (23 m when the device is powered at 24 V), the Doppler Velocity Log (DVL) can determine the robot velocities as well as the altitude from the seabed. The average power drawn by the ADCP/DVL pinging at its maximum rate at maximum altitude is 3 W, with a constant background power consumption equal to 2.2 W. The robot's processor connects to the ADCP/DVL device through an RS-232 serial port. The selected output format is PD0, which is a binary format that provides the most possible information. Table 3.17 summarizes the main characteristics of SOTAB-I ADCP.

UMS

SOTAB-I is equipped with an underwater mass spectrometer (UMS). The UMS instrument used for the SOTAB-1 deployments contained a 200 amu linear quadrupole mass analyzer (E3000, Inficon, Inc., Syracuse, New York). Table 3.18 provides the specifications of SRI International membrane introduction mass spectrometry (MIMS) system.

Introduction of analytes into the mass spectrometer occurs through a hydrophobic and nonporous high-pressure polydimethyl siloxane (PDMS) membrane introduction system, pressure tested to a depth of 2,000 m. Water samples are placed in contact with the semipermeable membrane, usually at a constant flow rate. The transport of dissolved gases and relatively nonpolar volatile organic compounds (VOCs) through these membranes is compound specific and temperature dependent, but typically requires that the solute dissolves into the membrane, diffuses through it, and finally evaporates into the mass spectrometer. Once in the mass spectrometer vacuum chamber, the neutral gas-phase analytes are (1) ionized by electron impact, (2) sorted by their mass-to-charge (m/z) ratios (typically $z = 1$), and (3) detected to create a mass spectrum. The membrane interface used in this system provides parts-per-billion level detection of many VOCs and subparts-per-million detection limits for many dissolved light stable gases.

The membrane probe assembly consists of a hollow fiber PDMS membrane stretched and mounted on a sintered Hastelloy C rod. One end of the supported membrane is capped with a polyetheretherketone (PEEK) rod; the other end is connected to the vacuum chamber via stainless steel tubing. The membrane assembly is inserted into a steel heater block that houses a thermocouple and heater cartridges for controlling sample and membrane temperature ($\pm 0.1\,^{\circ}\mathrm{C}$). A magnetic piston pump draws ambient water into the sample tubing, through the membrane probe assembly, and back to the environment.

3.2.2.8 Emergency

Since the communication with the robot may be lost for various reasons, such as a software crash or a hardware problem, commanding the robot may be no longer possible. In this particular case, a second method based on the use of an acoustic weight cutoff unit, which is completely independent from the circuit of the system, can be utilized for emergency surfacing. An additional radio beacon and a blinker flasher light are installed in the robot to assist in finding it in such circumstances.

3.2.3 Software Description

The SOTAB-I performs its surveying tasks autonomously. The operating mode is selected by the user on board the mother ship at the beginning of the operation by means of a graphical user interface (GUI). Orders are transmitted to the underwater robot through the acoustic modem. On the robot side, oceanographic and dissolved substance data collected by the SOTAB-I are sent to the mother ship in real time through an acoustic modem. On the mother ship side, the GUI receives the data collected from SOTAB-I, stores them, and displays the most essential data to the user (Fig. 3.10). Data related to the spilled plume and underwater currents are processed not only for guidance and control of the SOTAB-I but also for the simulation and the prediction of plume behavior contributing to the decision-making process for the best deployment strategy of collecting and cleaning machines.

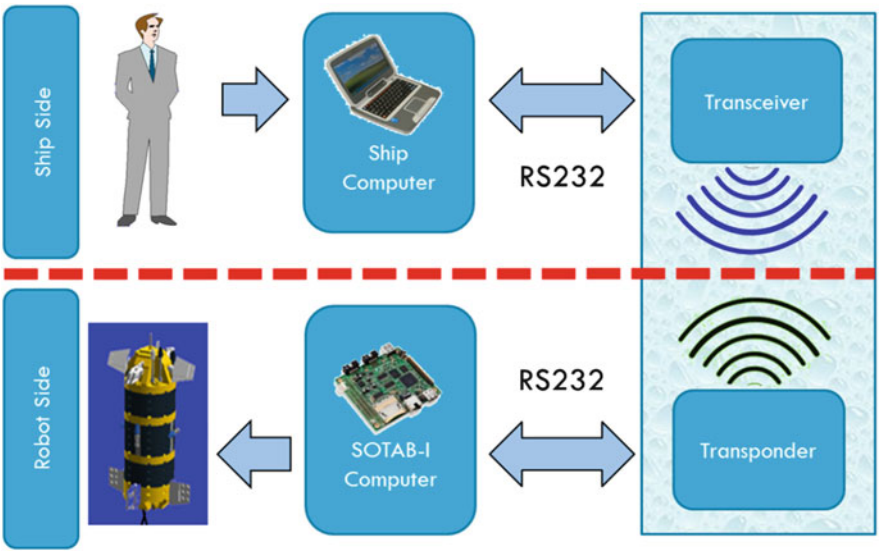

Fig. 3.10 Diagram of operation during at-sea experiments

3.2.3.1 Ship Computer

On board the ship, a portable computer running on Windows 7 operating system is employed. The integrated development environment (IDE) is Borland C++6. The GUI and the TrackLink will be executed. TrackLink is the software that comes with the USBL product.

TrackLink is used to determine the robot position and to manage the underwater communication. It connects to the external devices through an RS-232 serial interface (Fig. 3.11). TrackLink output data follows the LQF format. The data include information about the ship position and heading as well as the robot position and its depth. TrackLink and the ship GUI exchange information through virtual RS-232 serial ports. The ship GUI sends downlink data to the robot via the TrackLink software. From the GUI side, the Iridium module and the hydrophone are interfaced through a serial RS-232 interface. A joystick is interfaced through the USB port. The GUI (Fig. 3.12) has several roles that can be classified to three categories: display, guidance, and communication. The GUI shows the most important information about the robot status and its environment. It displays the robot position, orientation, and speed in addition to its actuators' status. Environmental data such as oceanographic data and substances' dissolutions are also displayed. Additionally, the GUI enables the selection of the operating mode and the manual control of the actuators. It gives the possibility to send a software emergency ascending order. The GUI combines interfaces for managing the Iridium satellite communication and the acoustic communication.

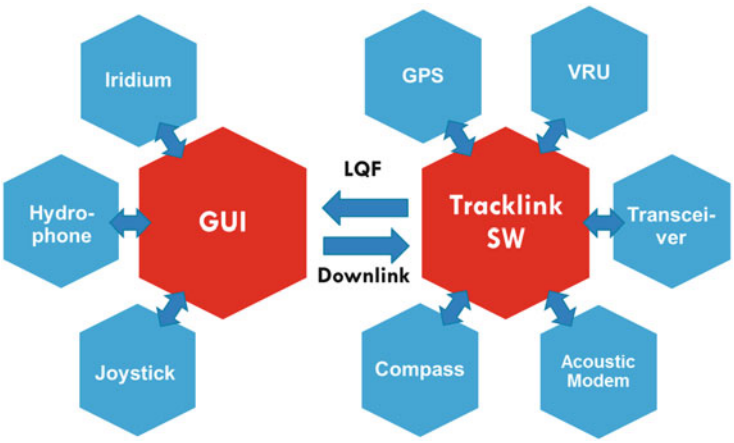

Fig. 3.11 Ship computer

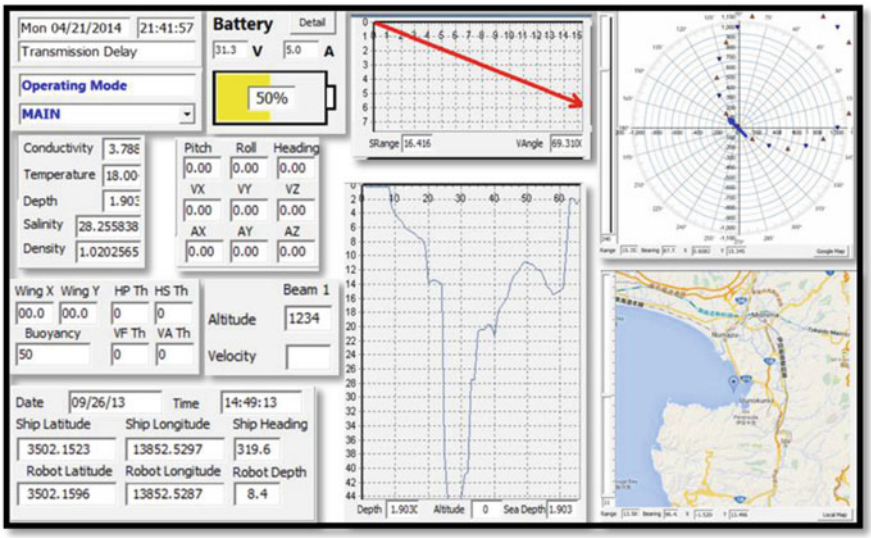

Fig. 3.12 Overview of SOTAB-I GUI

3.2.3.2 SOTAB-I Computer

The SOTAB-I program is running on the Windows XP embedded operating system. Borland C++ Builder 6.0 was selected as the integrated development environment (IDE) to develop the GUI. At the beginning of the operation, the magnet that is put on the magnetic switch is removed and the system is powered on. After the operating system is started, the executable program of the GUI is launched automatically. The average CPU usage when the program is fully executing is 3 %.

The robot processor connects to the sensors through RS-232 serial ports. Because a physical serial port can only be used by a single application at one time, a virtual serial splitter was employed to duplicate the serial data input (Fig. 3.13). One of the duplicated inputs is directed to a serial logger software to save raw data in a file for ulterior detailed analysis. Another one is sent to the main program for real-time processing. All sensors' data are saved by the GUI every 1 s in their corresponding files with their associated time, which makes it easier to synchronize at post-processing. A third clone of the serial input is directed to a third-party software that is specific to each sensor.

The GUI software was organized into a hierarchical order as shown in Fig. 3.14. In this multilayered architecture, responsibilities are distributed. Drivers are the software libraries that directly interface with the hardware and control it. They initialize the device and manage it. The driver layer contains drivers for peripherals such as DAC, ADC, I^2C interface, RS-232 interface, etc. The real-time operating system (RTOS) can run multiple tasks simultaneously. The task can exchange information through the global variables (Fig. 3.15). All tasks are executed peri-

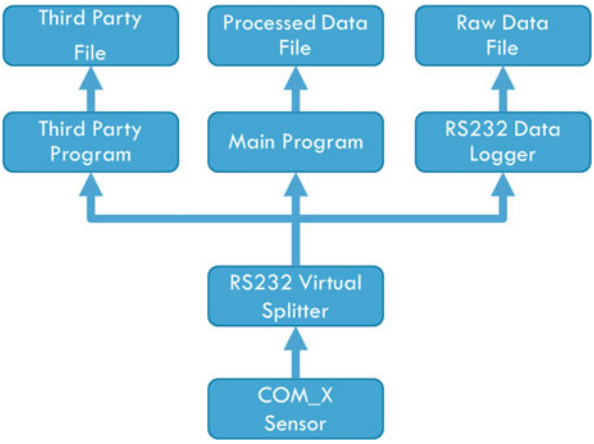

Fig. 3.13 Serial data acquisition

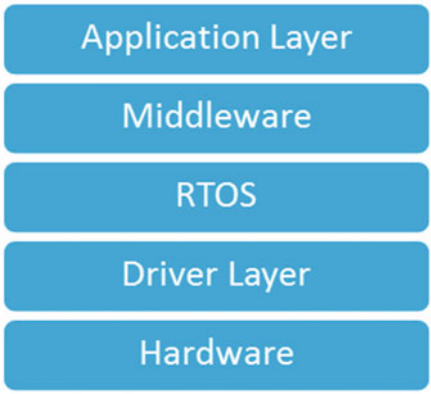

Fig. 3.14 Software architecture of SOTAB-I GUI

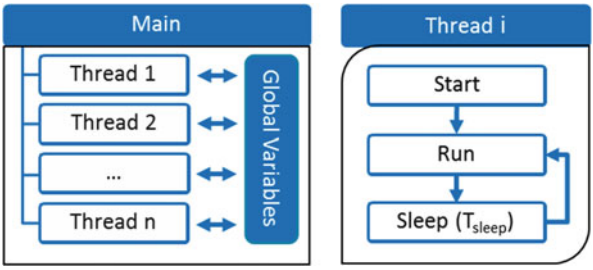

Fig. 3.15 Application layer, general structure of thread execution

odically. A sleep command is used to determine the frequency of the execution of the thread. At the beginning of the execution of the program, every task is initialized. The current thread runs sequentially through the instruction till the end. Then, the execution of the current thread is stopped until at least Tsleep has elapsed. The middleware layer provides services to the upper application to facilitate the communication, input/output, and data management. It is responsible for managing

serial communication and LAN and ensures process-to-process communication. The application layer contains all personalized programs of the robot.

The program is composed of several files that can be classified into three categories: the header files that include all the function definitions and predefined variables, the source files that include the program source of function, and the configuration files, which are the only files that need to be modified by the user.

3.2.3.3 Acoustic Communication

The acoustic data exchange format between the ship and the SOTAB-I is defined as shown in Fig. 3.16. Downlink data are used to command the SOTAB-I. In addition, it is used for sending the robot's absolute underwater position. For that reason, downlink data are sent continuously. At the beginning of the experiments, SOTAB-I and the ship computer's times are synchronized. Using the time stamp that is associated with each downlink data, it is possible to determine the shifting between the time in which the robot position was determined on the ship and the time when it was received by the robot. Uplink data include sensor data and actuator states to keep the user informed about the robot situation and the changes in its environment. Downlink data are also feedback on the uplink data to verify the authenticity of

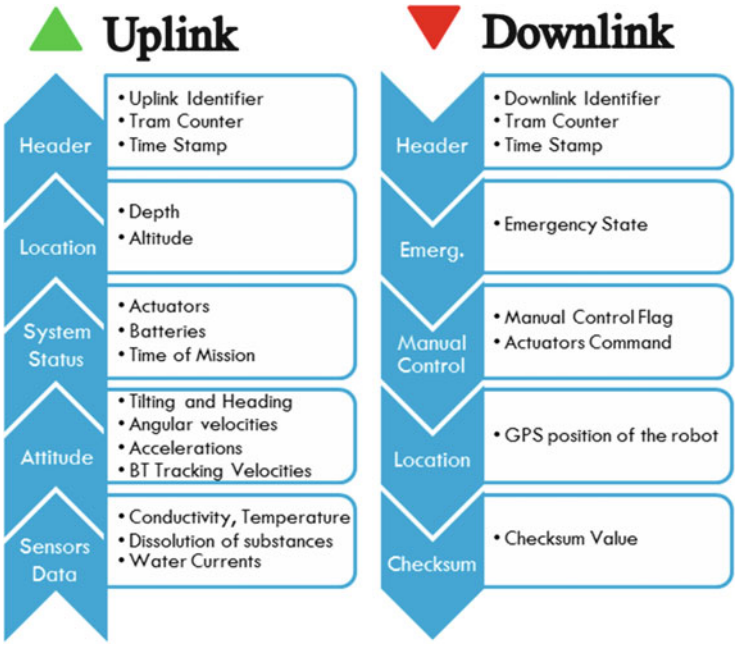

Fig. 3.16 Acoustic communication data frame

the communication and whether noise occurred during data submission. The ASCII format was selected for coding data. This gives the possibility to read and send the data simply by using a serial terminal. Additionally, data can be interpreted without a specific parser. The binary format gives the advantage of sending a bigger amount of data. However, uplink and downlink data exchange rates are enough to send all important data under the text format.

During the experiments, it was noticed that additional bytes are sometimes injected into the downlink data. Since the downlink data are used to control the actuators of the robot, noise injected into the data may lead to a misinterpretation of the orders and cause serious damage. For instance, if the robot receives an order to move the vertical thruster in the backward direction, the robot will start diving very fast to the seabed, and it may be impossible to recover it. To enhance the immunity of the system against mistaken orders caused by noise, a checksum algorithm was used for downlink data. The integer addition checksum was employed. It is a simple algorithm that reduces considerably the probability of undetected errors. It can detect all single bit errors and all error bursts of length 16 bits or less. The percentage of undetected 2-bit errors over the total number of 2-bit errors is less than 3 % for a message length equal to 80 bytes (Maxino and Koopman 2009).

3.3 SOTAB-I Guidance and Control

3.3.1 General Description

3.3.1.1 Operating Modes

Manual Mode

In this mode, the control of the robot will be performed manually through the GUI. Commands can range from simple orders to following a whole control scenario. This mode primarily enables us to test the robot's basic functions and to verify that all sensors and actuators as well as tracking and data transmission devices are working correctly.

Survey Mode

SOTAB-I has three main surveying modes. At the first stage, SOTAB-I performs the water column survey by adjusting its buoyancy. The rough mode is used to collect rough data on physical and chemical characteristics of plumes by repeating descending and ascending on an imaginary circular cylinder centered at the blowout position of oil and gas through the variation of buoyancy and movable wings' angles. Finally, in case the UMS detects a high concentration of any particular

substance, a precise guidance mode will be conducted to track and survey its detailed characteristics by repeating descending and ascending within the plume.

Photograph Mode

This mode enables us to have a large visual overview of the area around the blowout position of oil and gas by taking pictures of the seabed and making image mosaicking. SOTAB-I moves laterally using horizontal thrusters along diagonal lines of a polygon with a radius of 5 m centered on the blowout position of oil and gas.

3.3.1.2 Operating Zones

Based on the robot altitude from the seabed, the water column is divided into three zones, as illustrated in Fig. 3.17:

Normal Operation Zone

In this zone, the robot performs surveying in operational modes as well as the photograph mode. When the user on the mother ship decides to launch a specific operational mode, the GUI reads its associated ID and includes it in the downlink data that will be sent through the acoustic modem. The robot receives the data, identifies the requested mode, and executes it. At the end of the execution, the robot waits for the next downlink order.

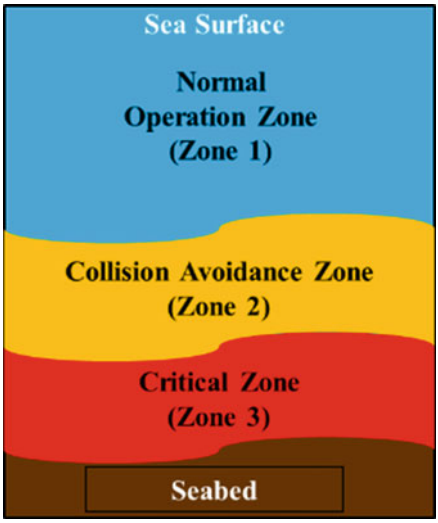

Fig. 3.17 Water column regions

Collision Avoidance Zone

This is the zone from which operation of the robot is judged to be somewhat dangerous because the robot is getting closer to the seabed. A collision avoidance maneuver based on PID control of vertical thrusters is used to smoothly stabilize the robot above a predefined critical altitude.

Critical Zone

Operation of the robot in this zone is very dangerous and presents a risk that the robot can hit the seabed, which may lead to heavy damage to the robot and especially to the ceramic transducer of the DVL. The altitude of the critical zone is adaptive and is determined based on the vertical speed of the robot and its altitude. The control program calculates the time needed to reach the seabed based on the vertical speed value. For the case in which the time to reach the seabed becomes less than a specified time limit, the thrusters are activated. This enables the robot to have enough time to decelerate the robot. The thrusters are also automatically activated in the case where the robot altitude goes below a specified critical value.

3.3.1.3 Control Priorities

The control priorities are shown in Fig. 3.18. The emergency order has the highest priority. A state of emergency is flagged when the robot battery runs below a predefined threshold. At the beginning of each mission, the mission timer is reset. When the timer reaches the maximum mission time, the emergency is activated. The emergency state can also be sent through downlink data when an abnormality is detected in the control program or in the uplink data received. Overheating, humidity, and high currents can also be added, but they are not currently implemented in the software. When the emergency is activated, the program interrupts the control algorithm and sets the neutral buoyancy to its maximum value. The

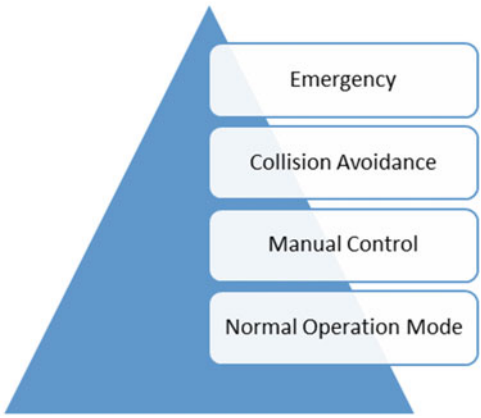

Fig. 3.18 Control priorities

data logging resumes normally and sensors are kept powered on, except in the case when the power of the system becomes too low. It is important to mention here that this emergency is a software emergency, and it is different from the emergency encountered by dropping the ballast weight. The second-place priority is the collision avoidance program. The collision avoidance uses only the thrusters. Thus, if the control program does not involve the control of the thrusters, it will keep executing. Otherwise, the thruster command from the control program will be ignored, and only the collision avoidance command will be considered. Manual control comes next. On the sea surface, only the manual control through Wi-Fi is counted, while the acoustic control is ignored. When the robot is underwater, the control through radio waves becomes impossible, and the acoustic communication is used instead. The robot is able to know its position regarding water level through the GPS status flag. When the robot is connected to Wi-Fi, the manual control can be performed either through GUI directly or through a joystick connected to the UDP port. The control of the robot through downlink data is explained in Sect. 3.2.3.3. Finally, if none of the higher-priority algorithms are flagged, the robot performs its designated operating mode described in Sect. 3.3.1.1.

3.3.2 Equations of Motion

Using the coordinate system illustrated in Fig. 3.19, where the origin of the coordinates is set at the center of gravity, the following equation of motion in the

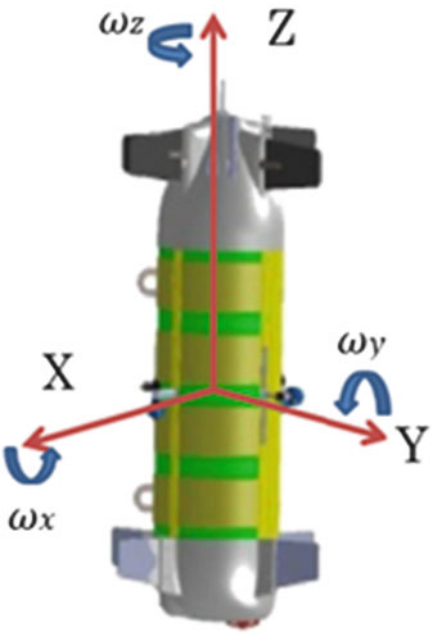

Fig. 3.19 Body-fixed coordinate system

body-fixed coordinates is expressed, where the symbols A_{11}, A_{21}, ... and I_{XX}, I_{XY}... are defined as the added mass and the moment of inertia (Azuma and Nasu 1977). Added mass is computed by the Hess-Smith method (Hess and Smith 1964) and the moment of inertia is calculated from the equipment layout. Other parameters are defined in Table 3.4.

$$
\begin{pmatrix}
\mathrm{M}+\mathrm{A}_{11} & 0 & 0 & 0 & \mathrm{A}_{51} & 0 \\
0 & \mathrm{M}+\mathrm{A}_{22} & 0 & \mathrm{A}_{42} & 0 & 0 \\
0 & 0 & \mathrm{M}+\mathrm{A}_{33} & 0 & 0 & 0 \\
0 & \mathrm{A}_{24} & 0 & I_{XX}+A_{44} & -\mathrm{I}_{\mathrm{YX}} & -\mathrm{I}_{\mathrm{ZX}} \\
\mathrm{A}_{15} & 0 & 0 & -\mathrm{I}_{\mathrm{XY}} & \mathrm{I}_{\mathrm{YY}}+\mathrm{A}_{55} & -\mathrm{I}_{\mathrm{ZY}} \\
0 & 0 & 0 & -I_{XZ} & -\mathrm{I}_{\mathrm{YZ}} & \mathrm{I}_{\mathrm{ZZ}}+\mathrm{A}_{66}
\end{pmatrix}
\begin{pmatrix}
\dot{U}_X \\ \dot{U}_Y \\ \dot{U}_Z \\ \dot{\omega}_X \\ \dot{\omega}_Y \\ \dot{\omega}_Z
\end{pmatrix} =
$$

$$
\begin{pmatrix}
\left\{ \begin{array}{r} -F_1 \sin\Theta + F_{HX} + (M+A_{22})\, U_Y\omega_Z - A_{22}W_Y\omega_Z + A_{33}W_Z\omega_Y \\ + A_{24}\omega_X\omega_Z - (M+A_{33})\, \omega_Y\omega_Z \end{array} \right\} \\
\left\{ \begin{array}{r} F_1 \cos\Theta \sin\Phi + F_{HY} - (M+A_{11})\, U_X\omega_Z + (M+A_{33})\, U_Z\omega_X \\ + A_{11}W_X\omega_Z - A_{33}W_Z\omega_X - A_{15}\omega_Y\omega_Z \end{array} \right\} \\
\left\{ \begin{array}{r} F_1 \cos\Theta \cos\Phi + F_{HZ} + (M+A_{11})\, U_X\omega_Y - (M+A_{22})\, U_Y\omega_X \\ - A_{11}W_X\omega_Y + A_{22}W_Y\omega_X - A_{24}\omega_X^2 + A_{15}\omega_Y^2 \end{array} \right\} \\
\left\{ \begin{array}{r} F_2\,(y_B \cos\Theta \cos\Phi - z_B \cos\Theta \sin\Phi) + M_{HX} + (A_{22}-A_{33})\, U_Y U_Z \\ + A_{33}U_Y W_Z - A_{22}U_Z W_Y + A_{15}U_X\omega_Z + A_{24}U_Z\omega_X \\ - A_{15}W_X\omega_Z + (I_{YY} - I_{ZZ} + A_{55} - A_{66})\, \omega_Y\omega_Z \end{array} \right\} \\
\left\{ \begin{array}{r} F_2\,(-z_B \sin\Theta - x_B \cos\Theta \cos\Phi) + M_{HY} - (A_{11}-A_{33})\, U_X U_Z \\ - A_{33}U_X W_Z + A_{11}U_Z W_X - A_{24}U_Y\omega_Z - A_{15}U_Z\omega_Y \\ + A_{24}W_Y\omega_Z - (I_{XX} - I_{ZZ} + A_{44} - A_{66})\, \omega_X\omega_Z \end{array} \right\} \\
\left\{ \begin{array}{r} F_2\,(x_B \cos\Theta \sin\Phi + y_B \sin\Theta) + M_{HZ} + (A_{11}-A_{22})\, U_X U_Y \\ - (A_{15}+A_{24})\,(U_X\omega_X - U_Y\omega_Y) + A_{22}U_X W_Y - A_{11}U_Y W_X \\ + A_{15}W_X\omega_X - A_{24}W_Y\omega_Y + (I_{XX} - I_{YY} + A_{44} - A_{55})\, \omega_X\omega_Y \end{array} \right\}
\end{pmatrix}
\tag{3.1}
$$

F_1 and F_2 are given by the following equations:

$$\boldsymbol{F}_1 = \boldsymbol{\rho g V_B} - \boldsymbol{Mg} + \boldsymbol{F_B} \tag{3.2}$$

$$\boldsymbol{F}_2 = \boldsymbol{\rho g V_B} + \boldsymbol{F_B} \tag{3.3}$$

The motion of the robot can be simulated by solving Eq. 3.1 using the Newmark-β method. Using this simulation, programs of guidance and control are constructed and the required times for operation are estimated.

For the rough guidance mode, a set of target points along the circles at the top and the bottom of a circular cylinder are given to perform line tracking between a point at the top of the circular cylinder and a point at the bottom of the circular

Table 3.4 Definition of parameters of the equation of motion

Symbols	Definition
(X, Y, Z)	Body-fixed coordinates
(U_X, U_Y, U_Z)	Robot velocity
(W_X, W_Y, W_Z)	Water current velocity
(ω_X, ω_Y, ω_Z)	Angular velocities
$A_{i,j}$ (i, j=1∼6)	Added mass
M	Robot mass
(X_B, Y_B, Z_B)	Buoyancy center
F_B	Buoyancy
(F_{HX}, $F_{HY,}F_{HZ}$)	Hydrodynamic forces
(M_{HX}, $M_{HY,}M_{HZ}$)	Hydrodynamic moments
ρ	Water density
g	Gravity acceleration
V_B	SOTAB-I's volume
$I_{i,j}$ (i,j=X, Y, Z)	Moment of inertia
θ	Pitch angle
ϕ	Roll angle
ψ	Azimuth angle
$\dot{()}$	Derivative with respect to time

cylinder. Let us define ($X_{E,i}$ $Y_{E,i}$ $Z_{E,i}$) and ($X_{E,SOTAB}$ $Y_{E,SOTAB}$ $Z_{E,SOTAB}$) as the target point and the position of SOTAB-I, respectively, in the Earth-fixed coordinate. If we define (X_p, Y_p, Z_p) as the offset of the present position from the target point in the body-fixed coordinate, (X_p, Y_p, Z_p) can be obtained as follows.

$$\begin{pmatrix} \boldsymbol{X_p} \\ \boldsymbol{Y_p} \\ \boldsymbol{Z_p} \end{pmatrix} = \boldsymbol{T_B} \begin{pmatrix} \boldsymbol{X_{E,i}} - \boldsymbol{X_{E,SOTAB}} \\ \boldsymbol{Y_{E,i}} - \boldsymbol{Y_{E,SOTAB}} \\ \boldsymbol{Z_{E,i}} - \boldsymbol{Z_{E,SOTAB}} \end{pmatrix} \tag{3.4}$$

$$T_B = \begin{pmatrix} \cos\Theta\cos\Psi & \cos\Theta\sin\Psi & -\sin\Theta \\ \cos\Psi\sin\Phi\sin\Theta - \cos\Phi\sin\Psi & \cos\Phi\sin\Theta\sin\Psi + \cos\Phi\sin\Psi & \cos\Theta\sin\Phi \\ \cos\Phi\cos\Psi\sin\Theta + \sin\Phi\sin\Psi & \cos\Phi\sin\Theta\sin\Psi - \cos\Psi\sin\Phi & \cos\Phi\cos\Theta \end{pmatrix} \tag{3.5}$$

A pair of wing angles is obtained using the PID control algorithm based on the offset components X_p and Y_p. The amount of buoyancy generated by the buoyancy control device is obtained using the PID control algorithm based on the offset Z_p.

3.3.3 *Depth Control*

In order to dive and perform surveying properly, SOTAB-I requires an adequate depth control. The depth control is performed by controlling the buoyancy control device. Three types of depth control methods are applied in SOTAB-I.

3.3.3.1 PID Depth Control

The first method for depth control is the PID control algorithm, which is shown in Fig. 3.20. The input of this control system is the target depth D_t,, and the output is the current depth, D. The difference between D_t and D is represented as the error e. The value of the error is input to the PID controller, which includes proportional, integral, and derivative actions. The PID controller gives a manipulated value of target buoyancy B_t as its output, which will be received by the buoyancy control device. Then the buoyancy control device will make an adjustment to the robot's buoyancy B. The results of the application of this controller in Toyama Bay experiments are discussed in Sects. 3.3.5.1 and 3.3.5.2.

Figure 3.25 in Sect. 3.3.5.1 shows that for target depth, $D_t = 300$ m, there was an approximately 130 m overshoot. However, there was a roughly 34 m overshoot for the target depth, $D_t = 150$ m, as shown in Fig. 3.28 in Sect. 3.3.5.2. The disadvantage of the PID depth control is that it is not suitable for covering long-distance dives, since this would result in a very large overshoot. This is attributed to the difficulty of tuning the parameters and the many external factors affecting performance such as temperature, salinity, and the condition of neutral buoyancy. However, the PID controller has the advantage of a fast response and good stability when it is applied around the target depth.

3.3.3.2 Depth Control with Time Estimation

The second control method is depth control with time estimation, or T_c vs. T_r control.

The CTD sensors installed in SOTAB-I enables measurement of the depth D and the vertical speed S of the robot. At every moment, it is possible to have an

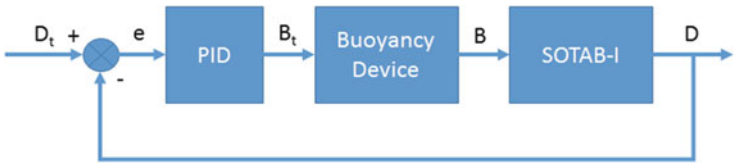

Fig. 3.20 Block diagram of PID controller for depth control

estimation of the time needed to reach the target depth T_r, at the current buoyancy level. In addition, using the buoyancy variation model based on the experimental data, and the experiments performed by SKE, the time T_c needed to change the robot buoyancy level from its current value to the neutral buoyancy condition can also be estimated.

This depth control method is based on the continuous estimation of the time to reach T_r and the time to change T_c.

- The case of estimated $T_r > T_c$: this means that it is still possible to increase the vertical speed of the robot since there will be enough time to change the buoyancy to its neutral level. Hence, the target buoyancy value is decreased.
- The case of estimated $T_r \leq T_c$: this means that there is still just enough time to change the buoyancy to the neutral level before the robot reaches its target depth. Hence, the buoyancy of the robot is increased progressively.

The time error margin T_m is also introduced in the estimation. T_m is used to compensate some error in the control mechanism of the buoyancy device. The condition for stopping increasing the robot vertical speed is when $T_r = T_c + T_m$.

This depth control method has the advantages of using the maximum buoyancy variation speed while reaching the target depth accurately. This method also allows some margin of inaccuracy in the determination of the neutral buoyancy value.

Depth control with time estimation consists of three parts:

1. Time to reach estimator

   The purpose of this part is to estimate the time needed to reach the target depth from the current depth based on the current speed of the robot.

   Input: D (m), D_t (m), and S (m/s)
   Output: T_r (s)
   Algorithm:

   - Read input parameters (D, D_t, S)
   - If ($S! = 0$) $T_r = ((D_t – D) / S)$
     Else $T_r = 9999$

2. Time to change estimator

   The purpose of this part is to estimate the time needed for changing the robot buoyancy level from the current level to the neutral buoyancy level.

   Input: B (%) and D (m)
   Configuration: B_n (%) and B_m (%)
   Output: T_c (s)
   Algorithm:

   - Read input parameters (B, B_n, D)
   - $R_D = D/700$
   - If ($B > B_n + B_m$) $T_c = -15.122\,(B_n – B)$

– Else if $(B < B_n - B_m)$

$$T_c = 0.0015R_D\left(B_n^3 - B^3\right) - 0.2688R_D\left(B_n^2 - B^2\right) + (15.725 + (34.065 - 15.725)\,R_D)\,(B_n - B)$$

– Else $T_c = 0$

R_D is the ratio used to interpolate the buoyancy model based on experimental data.

3. Buoyancy control

The purpose of this part is to determine the target buoyancy value based on the results of the time to reach and the time to change the estimator.

Input: B (%), T_c (s), T_r (s)
Configuration: B_n (%), B_m (%), D_m (m) , T_m (s)
Output: B_t (%)
Algorithm:

– Read input parameters (B, T_c, T_r)
– If $(T_c < (T_r – T_m))$ $B_t = B – 0.3$
Else $B_t = B + 1$
– If $(B_t > (B_n + B_m))$ $B_t = B_n + B_m$

The buoyancy error margin B_m and depth error margin D_m are introduced into the buoyancy control. They are used to compensate for some error in the control mechanism of the buoyancy device. A block diagram of the depth control with time estimation is shown in Fig. 3.21. In this figure, there is a dotted line connecting the output buoyancy B with the depth D. This indicates that the effect of buoyancy level change is to cause a change of robot depth.

The simulation of depth control with time estimation is shown in Fig. 3.22. The simulation started at a buoyancy level of 50 % and the water depth was equal to

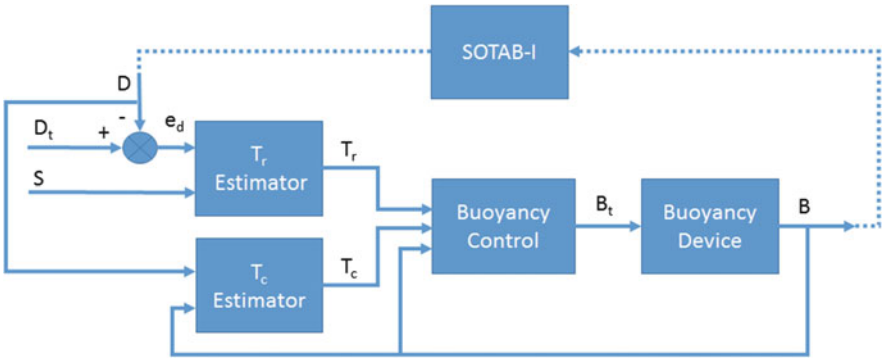

Fig. 3.21 Block diagram of PID controller for depth control

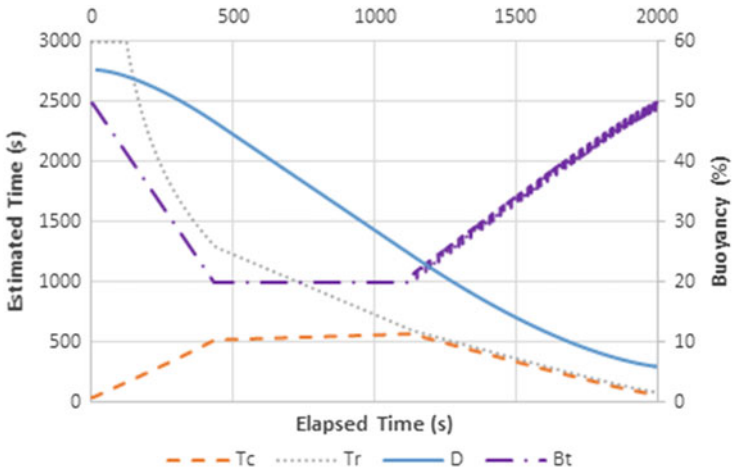

Fig. 3.22 Simulation of depth control with time estimation

0 m. With the buoyancy level equal to neutral buoyancy, then $T_c = 0$s. The value of T_r was very large because the depth was 0 m. Since $T_r > T_c$, the buoyancy control device reduced the buoyancy level. As SOTAB-I's buoyancy level was decreasing and the depth was increasing, T_c became larger and T_r became smaller. When the buoyancy level was stable at the minimum buoyancy level of 20 %, T_c increased only slightly. While at the minimum buoyancy level, SOTAB-I was diving with maximum speed, causing T_r to decrease at a faster rate than before. When $T_c \geq T_r - T_m$, the buoyancy control device started to increase the buoyancy level again. As the buoyancy level was increasing toward the neutral buoyancy level, the value of T_c was decreasing. T_r was still decreasing as the robot was still descending, but as the buoyancy level was getting closer to neutral buoyancy, the SOTAB-I descending speed became slower. Finally, the T_c and T_r were almost zero when the buoyancy level reached the neutral buoyancy level and the robot reached the target depth. Figure 3.31 in Sect. 3.3.5.3 shows the result of a sea-based experiment of SOTAB-I in Toyama Bay, where depth control with time estimation was applied. We found that SOTAB-I could reach the target depth with little overshoot.

In principle, this control method compares the time T_r needed to reach the target depth at the current buoyancy level, with the time T_c needed to change the robot buoyancy level from the current value to the neutral buoyancy level at any time during the operation. From this comparison, the buoyancy device will make an adjustment of the buoyancy level of the robot under the rule that T_c should not be larger than T_r. By doing so, SOTAB-I will always have enough time to change its buoyancy to reach the target depth. It is thus very reliable to apply the depth control with time estimation for long-distance dives. However, because the control algorithm is based on if-then-else rules, there will be oscillations when reaching the target depth. That is the reason why the PID controller is needed to achieve stability at the target depth. Hence, the combined control methods are used.

3.3.3.3 Progressive Depth Control

The third control method is progressive depth control. This method combines both of the previously explained two methods and improves their performance. It is also combined with altitude control by using DVL to detect the altitude of the robot from the seabed. This control method is very useful because sometimes SOTAB-I needs to do surveying very close to the seabed.

The progressive depth control strategy applied for the descending condition consists of four steps, as shown in Fig. 3.23, where steps 1–3 adopt the depth control with time estimation method, while step 4 adopts the PID depth control. The simulation result is shown in Fig. 3.24. In this simulation, the target depth D_t was set equal to 500 m, certain zone limit $D_{CZ} = 400$ m, depth margin $D_m = 1$ m, neutral buoyancy $B_n = 50\,\%$, and target altitude $A_t = 3$ m.

Step 1: The robot dives with a fast speed until the depth of the robot reaches the certain zone limit D_{CZ}.

The certain zone limit is the region where we are sure that the seabed will not be detected. The depth of the certain zone is input by the user on board before starting the descent. SOTAB-I will start to detect the seabed when the seabed is within the maximum detection range of the DVL, which is equal to 24 m altitude. In this first step, the depth control with time estimation scheme is used. At first, the buoyancy control device will decrease the buoyancy. After the buoyancy level becomes lower than the neutral buoyancy of the robot, SOTAB-I will start diving. The buoyancy control device will continue to reduce its buoyancy level down to 20 %, which is set as the minimum buoyancy level of the buoyancy control device, with maximum speed. Then it will increase again its buoyancy level close to the neutral buoyancy level, as shown in the step 1 in Fig. 3.24. The purpose of this strategy is that the robot should have enough time to change its buoyancy level to its neutral buoyancy when reaching the target depth. In this step, the target depth D_t is set as a fixed value, which is equal to the certain zone limit plus the DVL range R_{DVL}, minus the target altitude A_t.

Step 2: When the robot reaches the certain zone limit, the variable target depth control is started.

After passing the certain zone limit, there is a chance that the DVL will detect the seabed. Therefore, from this viewpoint, the buoyancy change is limited up to the time needed to reach the target depth T_r. In this step, the depth control with time estimation is still being used. However, the target depth D_t is set equal to the current depth D plus the DVL range R_{DVL} minus the target altitude A_t. The target depth will continuously change as the depth D of the robot decreases. Hence, it is a depth control with variable target depth, as shown in step 2 in Fig. 3.24. At this point, the buoyancy level of SOTAB-I is already close to the neutral buoyancy. Therefore, there will not be much change in the buoyancy level to ensure that the robot is able to stop when reaching the target depth, as shown in step 2 in

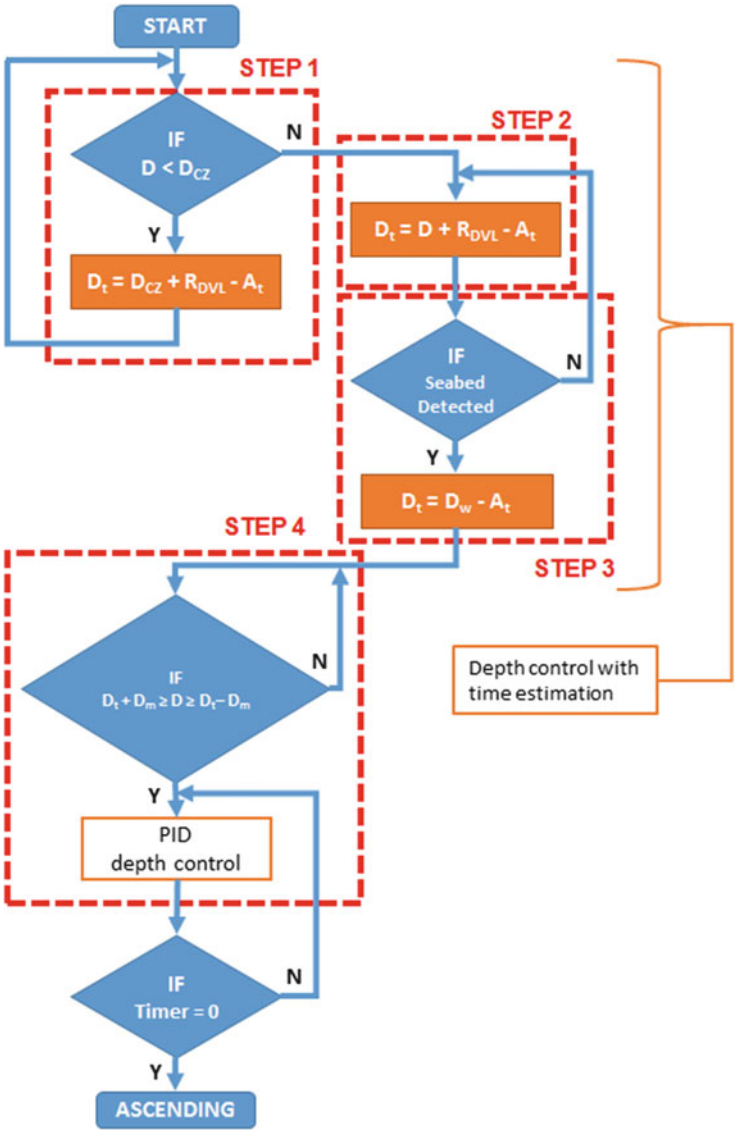

Fig. 3.23 Block diagram of progressive depth control

Fig. 3.6. As a result, the robot will dive at a steady speed, as shown in step 2 in Fig. 3.24.

Step 3: If the seabed is detected by DVL, the target depth D_t is set equal to the water depth D_w minus the target altitude A_t, as shown in step 3 in Fig. 3.23. The water depth D_w is defined as the sum of the depth D measured by CTD and the altitude

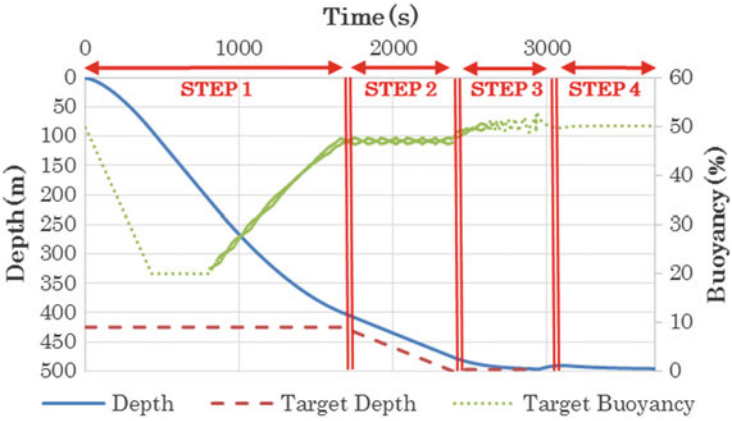

Fig. 3.24 Simulation of depth by progressive depth control

A measured by DVL. This step is also carried out by using the depth control with time estimation scheme.

Step 4: When the robot is within the range of the target depth plus or minus the depth margin D_m, the depth control method is switched from the depth control with time estimation to the PID depth control method. The depth margin D_m is usually set around 1 m as a compensation in the control mechanism of the buoyancy device. SOTAB-I will stay within the target depth for a certain period of time, which has been set on the timer. When the timer reaches zero, the robot will start ascending.

3.3.3.4 Heading Control

When performing the first stage of the survey mode, where SOTAB-I performs the water column survey by adjusting its buoyancy, it descends and gathers oceanographic data. There are two cases considered in this mode. The first one is to descend and ascend without controlling the movable wings, so SOTAB-I may drift along with the water current. The second one is to have heading control applied to control the direction of SOTAB-I during surveying. Using this heading control, it should be possible to control the trajectory of SOTAB-I during descending and ascending. It can also be used for rough guidance mode operation.

The heading control is applied for:

- X direction by multiplying the angle of wing inclination with the sine of the angle difference between the target azimuth and current yaw of SOTAB-I
- Y direction by multiplying the angle of wing inclination with the cosine of the angle difference between target azimuth and current yaw of SOTAB-I

In this case, the X direction refers to the east–west direction. The east direction is represented by positive values and the west direction is represented by negative values. The Y direction refers to the north–south direction. The north direction is represented by positive values and the south direction is represented by negative values.

The formulas for heading control are:

$$DELTX = \alpha \sin(\psi_t - \psi) \tag{3.6}$$

$$DELTY = \alpha \cos(\psi_t - \psi) \tag{3.7}$$

where α is the wing angle, ψ_t is the target azimuth, and ψ is the current azimuth (yaw), while *DELTX* and *DELTY* are the outputs for wing control.

The results of heading control will be discussed in Sect. 3.3.5.

3.3.4 Experimental Result

Field experiments of SOTAB-I have been conducted several times both in the towing tank and in the sea. In this section, only the experimental results in the towing tank in Osaka University, in Toyama Bay, and off Joetsu from 2014 to 2015 will be discussed in terms of depth control and heading control.

3.3.4.1 Field Test in Toyama Bay on the 28th of November 2014

On the 28th of November 2014, a field experiment of SOTAB-I was carried out in Toyama Bay, Japan. The experiment was performed by using a small ship of the National Institute of Technology, Toyama College, called Sazanami. The ship length is 16.0 m and its breadth is 4 m. In this experiment, the targeted depth was set as 300 m and target heading was set to 0° (north direction). The control algorithm used in this experiment was PID depth control. The performance of depth and heading control in this experiment can be seen in Figs. 3.25 and 3.26. As shown in Fig. 3.25, SOTAB-I reached 430 m depth before it started ascending. There was an approximate 130 m overshoot from the target depth. Figure 3.26 shows the orientation of SOTAB-I and Fig. 3.27 shows the horizontal position of SOTAB-I during this operation.

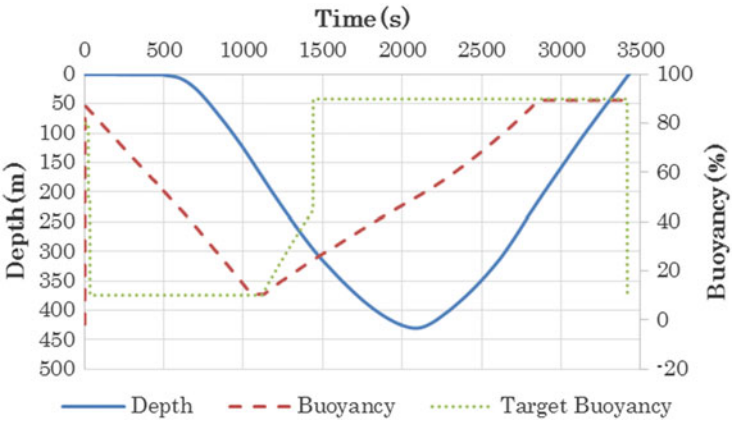

Fig. 3.25 Experimental result of depth control in Toyama Bay on the 28th of November 2014

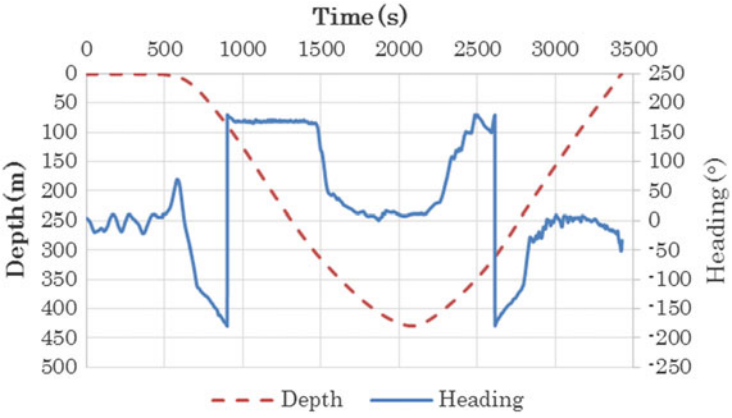

Fig. 3.26 Experimental result of heading control in Toyama Bay on the 28th of November 2014

3.3.4.2 Field Test in Toyama Bay on the 20th of March 2015

The next field experiment was also conducted in Toyama Bay, Japan, on the 20th of March 2015. The same ship, Sazanami, of the National Institute of Technology, Toyama College, was used again in this experiment. The experiment was carried out at position 36°51′N, 137°12′E with a water depth of around 700 m. In this experiment, the targeted depth was set as 150 m and target heading was set to 0° (north direction). As with the previous field test, only the PID control algorithm was used in this experiment. The performance of the depth control can be seen in Fig. 3.28. As shown in Fig. 3.28, SOTAB-I reached 184 m depth before it started ascending. There was an approximate 34 m overshoot from the target depth.

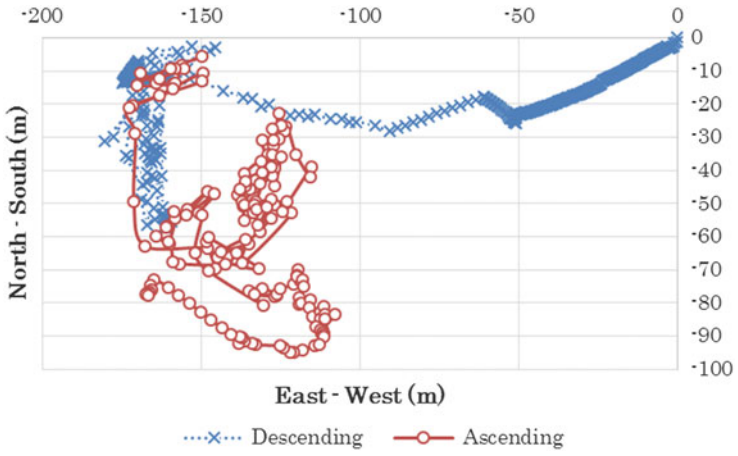

Fig. 3.27 Experimental result of horizontal positioning in Toyama Bay on the 28th of November 2014

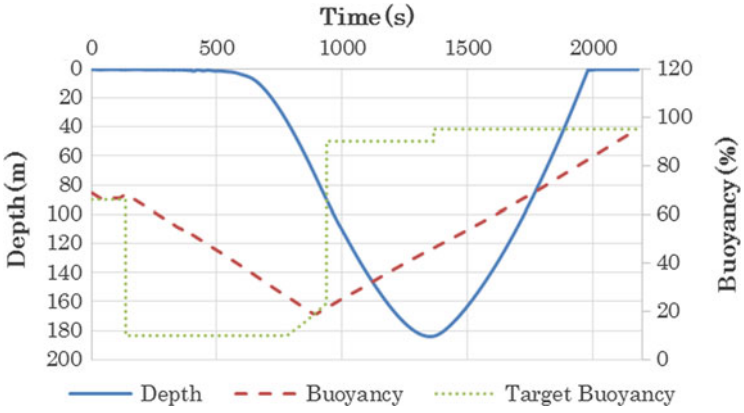

Fig. 3.28 Experimental result of depth control in Toyama Bay on the 20th of March 2015

During this experiment, the heading control was applied only when the robot was ascending, with the target azimuth 0° (north). Figure 3.29 shows the heading control performance in this experiment. When the robot started ascending, the robot's heading changed from about 50 to 0° and then was stable at around 337°. There was an approximate −23° shifting from the target azimuth. Figure 3.30 shows the horizontal position of SOTAB-I during this operation. Due to the effect of the water current, SOTAB-I moved mostly in the north and west directions.

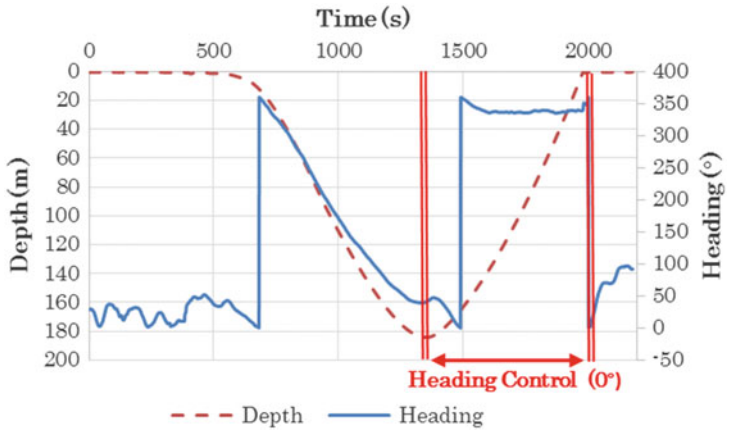

Fig. 3.29 Experimental result of heading control in Toyama Bay on the 20th of March 2015

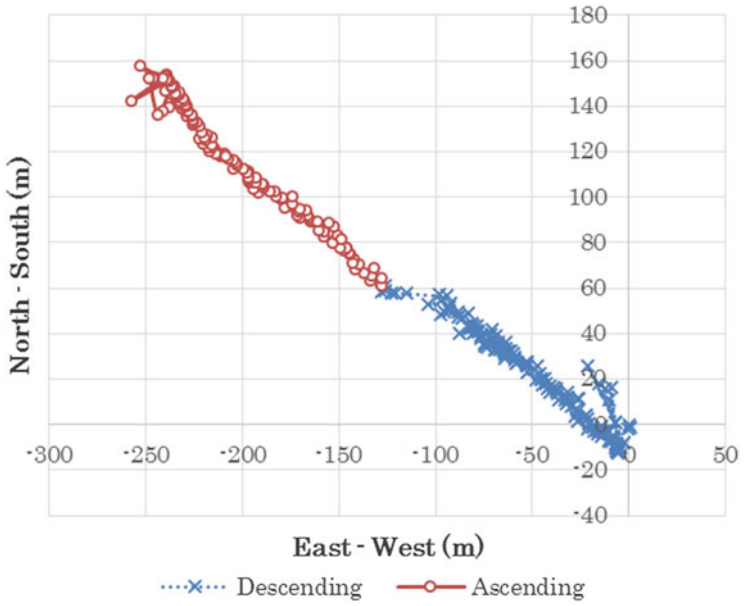

Fig. 3.30 Experimental result of horizontal positioning in Toyama Bay on the 20th of March 2015

3.3.4.3 Field Test in Toyama Bay on the 11th of June 2015

Another field experiment of SOTAB-I was carried out again in Toyama Bay, Japan, on the 11th of June 2015. However, this time the experiment was conducted using a bigger ship, the Wakashio-maru of the National Institute of Technology, Toyama

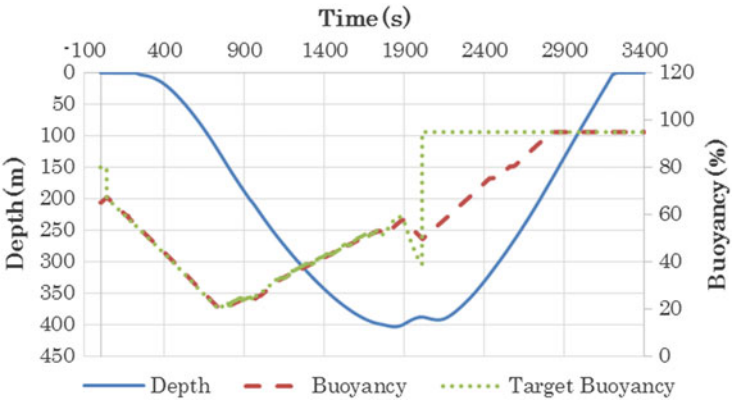

Fig. 3.31 Experimental result of depth control in Toyama Bay on the 11th of June 2015

College. The ship length is 53.59 m and its breadth is 10.0 m. The experiment site was located at 36°52′N, 137°11′E with a water depth of around 560 m.

In this sea experiment, the depth control with time estimation scheme was deployed, with a target depth of 400 m. The performance of the depth control is shown in Fig. 3.31. SOTAB-I was able to dive smoothly to the target depth of 400 m with very little overshoot. With the use of depth control with time estimation, the buoyancy device was able to adjust the buoyancy so that it could achieve neutral buoyancy when reaching the target depth. The challenge of this method is to accurately determine the value of neutral buoyancy, since there might be changes depending on the water depth and salinity. In this experiment, the timer scheme for the robot to start the ascent was not programmed in the control application; because of this, the emergency ascent mode was used to make the robot ascend. About 3 min after the robot reached the target depth, we decided to give the emergency ascent order. The order was input from the computer on board. When the emergency ascent order was given, the target buoyancy was set to 95 %, as shown in Fig. 3.31.

During this experiment, the heading control was applied only when the robot was ascending, with the target azimuth 60° (between north and west). Figure 3.32 shows the heading control performance in this experiment. When the robot started ascending, the robot's heading was already around 30°. Then it changed and stayed at approximately 35°. There was an approximate −25° shift from the target azimuth. The horizontal position of SOTAB-I during this operation is shown in Fig. 3.33. Since there was no heading control during descent, SOTAB-I drifted away along with the water current. When ascending, the robot was drifting because of the strong water current. However, the robot managed to move toward the direction between north and west eventually.

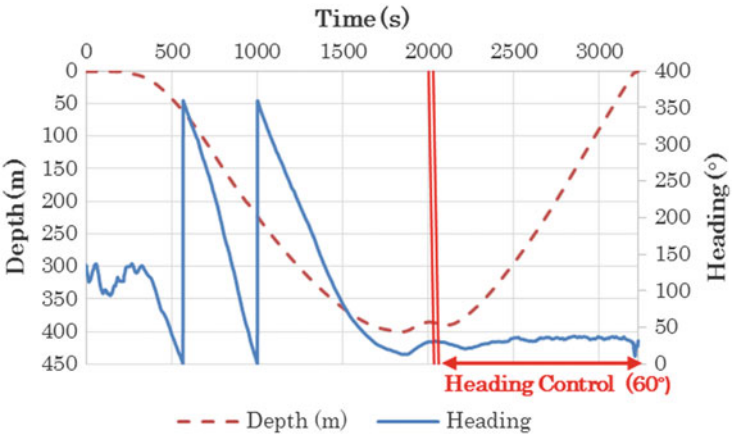

Fig. 3.32 Experimental result of heading control in Toyama Bay on the 11th of June 2015

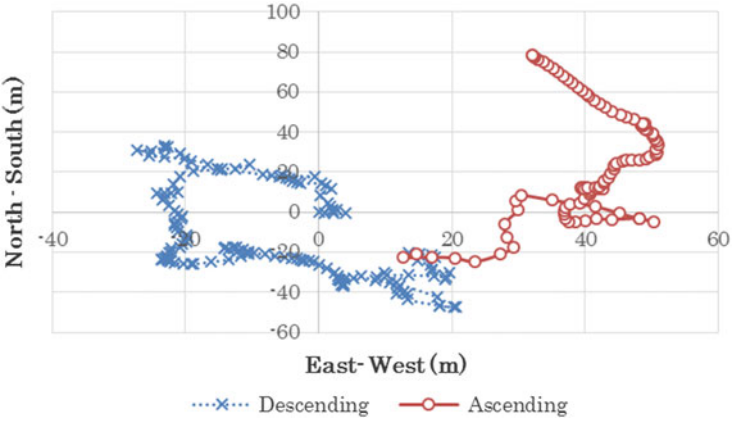

Fig. 3.33 Experimental result of horizontal positioning in Toyama Bay on the 11th of June 2015

3.3.4.4 Towing Tank Test at Osaka University on the 26th of August 2015

An experiment of the control performance of SOTAB-I was also carried out at the towing tank that belongs to the Naval Architecture and Ocean Engineering Department of Osaka University, Japan. The towing tank is 100 m in length, 7.8 m in width, and 4.35 m in depth. The purposes of this experiment were to check the whole system for the upcoming field experiments in the sea and to tune the progressive depth control.

Since the tank's depth is only 4.35 m, the second step of the progressive depth control was skipped. The target depth was set as 1.15 m, with a depth margin D_m of 0.25 m. It can be seen from Fig. 3.34 that the target buoyancy changed slightly from step 1 to step 3, which means that the control program was working. Then, the

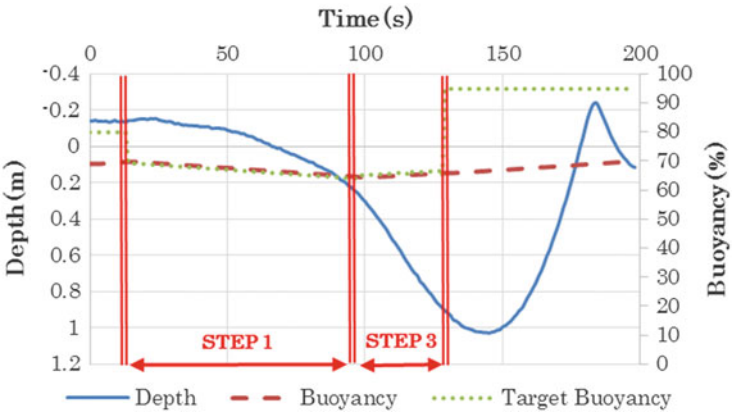

Fig. 3.34 Experimental result of depth control in Towing Tank on the 26th of August 2015

target buoyancy went to 95 % when the depth reached 0.9 m, because of the depth margin of 0.25 m from the target depth of 1.15 m.

3.3.4.5 Field Test off Joetsu, Niigata, on the 3rd of September 2015

A field test of SOTAB-I was also conducted in the sea, 20 nautical miles off Joetsu, Niigata, Japan, on the 3rd of September 2015. The experiment was carried out with use of Wakashio-maru of the National Institute of Technology, Toyama College, as the mother ship. In this experiment, SOTAB-I was equipped with the underwater mass spectrometer (UMS) to measure the methane gas concentration in the water. The targeted depth of this experiment was 700 m. Unfortunately, due to a water leakage inside the UMS, the operation was canceled midway, and SOTAB-I was commanded to come up to the surface using the emergency mode. Fortunately, some data were recovered.

The progressive depth control was deployed during this experiment. For safety reasons, the certain zone was set to 2.44 m. The target altitude was set at 3 m and the DVL range was 24 m. After reaching a water depth of 23.44 m, the control mode changed from step 1 to step 2, as shown in Fig. 3.35. As a result, SOTAB-I descended with a slow velocity. From this result, it can be seen that the progressive depth control worked well.

In this sea experiment, the heading control was applied for both descending and ascending processes. As shown in Fig. 3.36, the heading control of SOTAB-I did not work properly; it rotated all the time during descent and ascent. This might have happened because the robot was not in a balanced position due to the installation of the UMS. When installing the UMS into SOTAB-I, the dummy weight for the UMS was removed and additional buoyancy material was installed to balance the difference of weight between the UMS and the dummy weight. It is suspected that

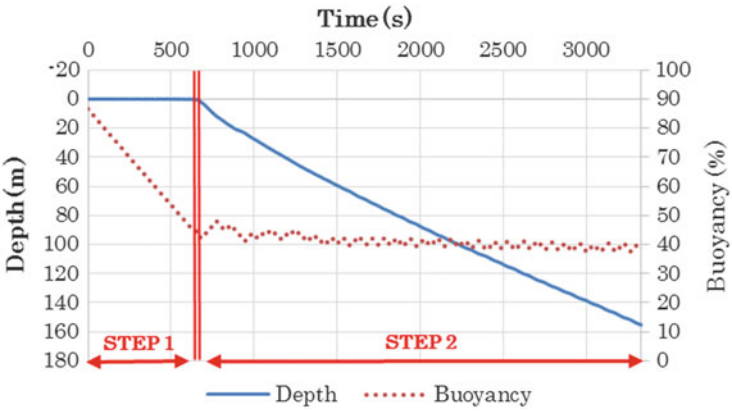

Fig. 3.35 Experimental result of depth control off Joetsu on the 3rd of September 2015

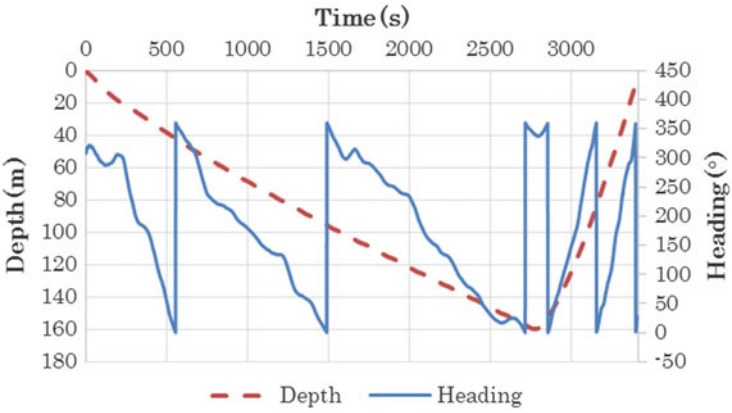

Fig. 3.36 Experimental result of heading control off Joetsu on the 3rd of September 2015

the position of the additional buoyancy material was off of the vertical centerline, causing the robot to tilt at a certain angle.

The horizontal position of SOTAB-I during this operation is shown in Fig. 3.37. Unfortunately, the USBL data obtained during this experiment was poor. Figure 3.37 shows that the horizontal position of SOTAB-I was scattered. However, this scattering of the data only occurred during descent. The data obtained during ascent were quite stable. This was also confirmed by the comparison of the depth data between the USBL and CTD, as shown in Fig. 3.38. The USBL data obtained during ascent were more stable and agreed well with the CTD depth data.

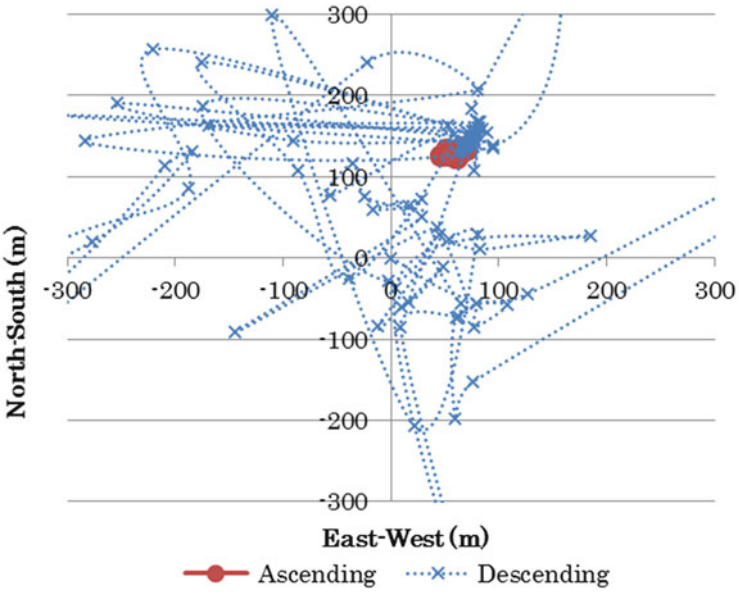

Fig. 3.37 Experimental result of horizontal positioning off Joetsu on the 3rd of September 2015

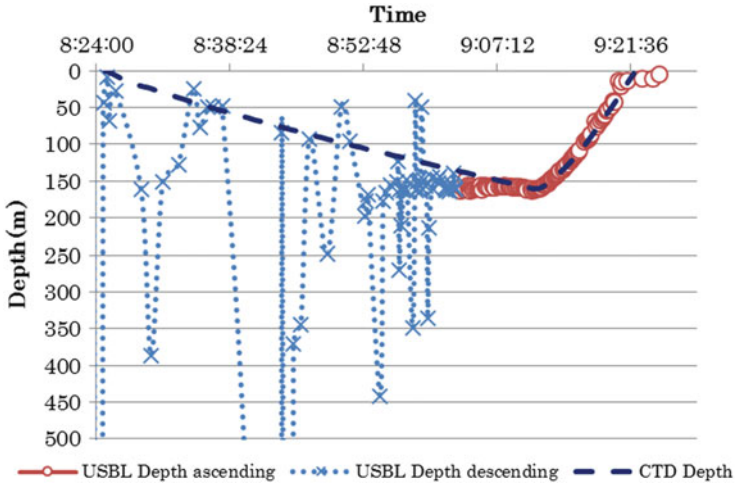

Fig. 3.38 Comparison of depth data off Joetsu on the 3rd of September 2015

3.3.5 Simulation

The simulation program was developed based on the equations of motion from Sect. 3.3.2. At first, the SOTAB-I model and the environmental model were predefined. The model of SOTAB-I considers the robot mass, added mass, length,

diameter, volume, buoyancy, center of buoyancy, center of gravity, pitch, roll, and azimuthal angle, while the environmental model includes the water depth, water density, gravitational acceleration, and also at a later point, the water current velocity as input parameters.

The dynamic analysis of the equations of motion leads to the outputs of the angular velocities, the translational velocities of SOTAB-I, and the effect of the water current velocity. Furthermore, by converting from body-fixed coordinates to an Earth-fixed coordinate system, the displacement of the robot in the X, Y, and Z directions can be obtained.

In the following subsections, examples of each control simulation will be discussed.

3.3.5.1 Depth Control

The depth control simulation is performed by using the simulation program based on the equations of motion in Sect. 3.3.2. The program is used to simulate the trajectory of SOTAB-I diving in the Z axis from a starting point at the sea surface until it reaches the sea surface again. In the simulation result, the depth of SOTAB-I at every second can be obtained. The program can also simulate the buoyancy of the robot during the operation, as well as the T_c, T_r, and the velocity of SOTAB-I in the Z axis, as shown in the examples in Figs. 3.39 and 3.40, respectively. In these examples, the target depth was set to 400 m and the progressive depth control was applied.

Figure 3.41 shows the comparison of the water depth of SOTAB-I from the experimental and simulated results. In this example, the data from the field experiment in Toyama Bay on the 11th of June 2015, are used for the comparison. From this comparison, it can be concluded that the simulation of the depth control is quite accurate.

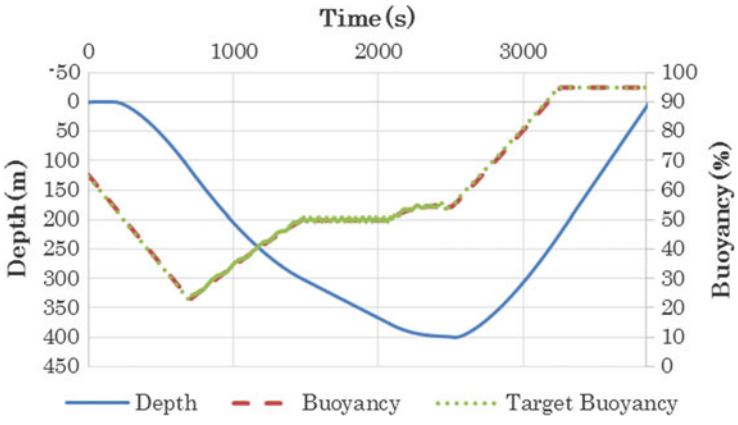

Fig. 3.39 Simulated results of buoyancy and depth in depth control

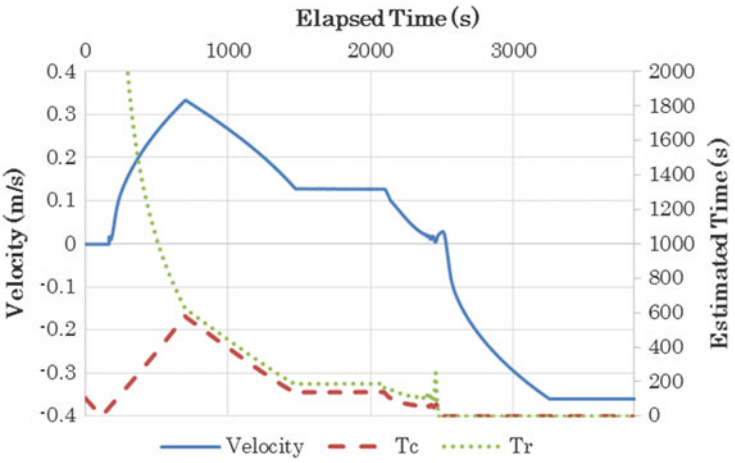

Fig. 3.40 Simulated results of *Tc*, *Tr*, and velocity in depth control

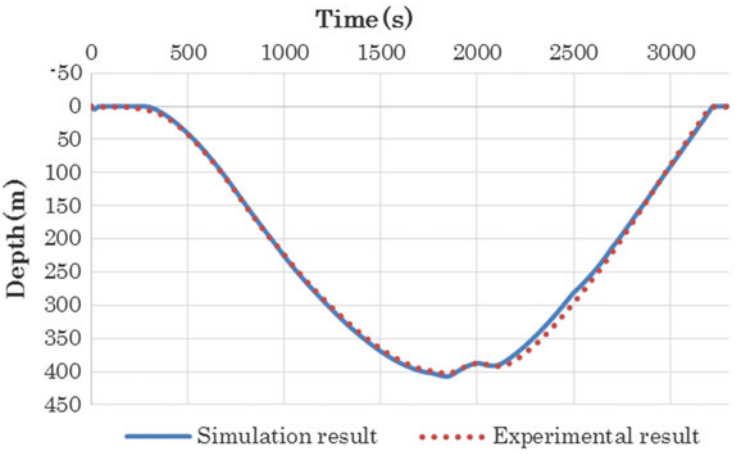

Fig. 3.41 Comparison of depth between simulation and experiment

3.3.5.2 Heading Control

The heading control simulation was performed by using the same program as the depth control simulation at the same time of the depth control simulation. The goal of this simulation was to simulate the SOTAB-I moving in the horizontal plane. Since the water current greatly affects the trajectory of the robot, the effect of the water current was considered in this simulation.

First, Fig. 3.42 shows the heading control simulation without the effects of water current taken into consideration. This figure shows the results from several simulations with different target headings. The north direction corresponds to the

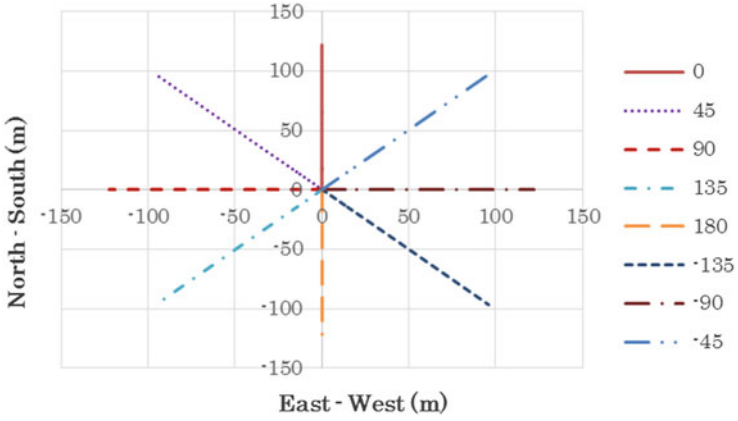

Fig. 3.42 Simulated results of heading control without water current

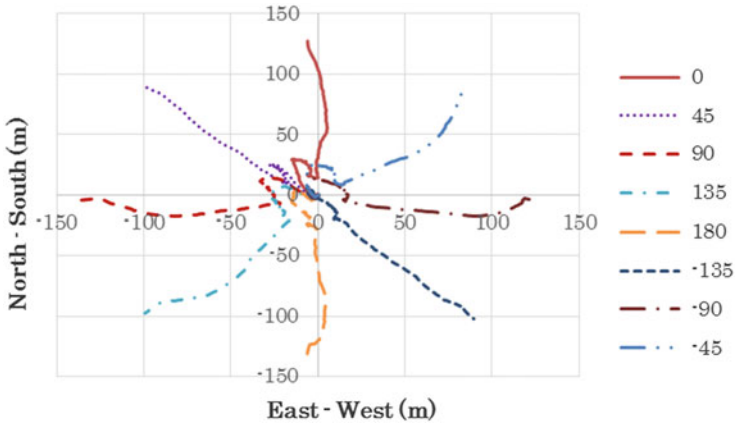

Fig. 3.43 Simulated results of heading control in water current

target heading of 0°, and then it goes counter clockwise with 90° corresponding to the westerly direction, 180° corresponding to the southerly direction, and −90° corresponding to the easterly direction.

Next, the water current was introduced into the simulation. In this simulation, a water current profile of 400 m water depth was used. The water current velocity and direction change according to depth were as shown in Figs. 3.43 and 3.44. The figures show the velocity and direction change in both east–west and north–south direction. In the shallower water depth, the water current was stronger in the north and west direction. As the depth increased, the water current became smaller and moved slightly toward the south and east directions (Fig. 3.43).

The simulated results for various target headings show that the robot was still able to move to each target heading with some curving due to the water current

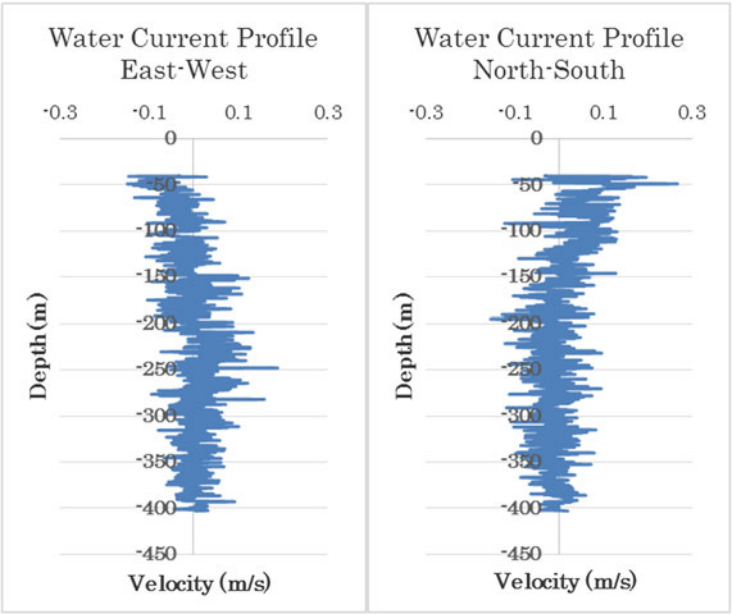

Fig. 3.44 Water current profile down to 400 m water depth

effect. Affected by the water current, the robot moved at first toward the north–west direction from the starting point (0,0). Then, as the robot descended, it changed direction toward the south–east. Since the water current velocity was smaller in the deep water, the robot was able to perform heading control, with a minimum effect from the water current, to its target heading. As the robot was ascending, it was affected by the stronger water current and moved toward the north–west.

The effect of water current on the position of SOTAB-I in the X–Z plane and in the Y–Z plane for a target heading of −135° are shown in Figs. 3.45 and 3.46, respectively, for two cases of heading control: heading control during descending and ascending and heading control only during descending. The target heading of −135° meant that SOTAB-I should have moved in the south–east direction. In Figs. 3.45 and 3.46, for the cases of heading control without water current, the robot moved starting from (0,0) directly toward the east (positive value) and south (negative value). We can see that the horizontal displacement during ascent was larger than that during descent. The movable wings used for the heading control are located on the top part of SOTAB-I, as shown in Fig. 3.20. These wings are directly against the water during ascent. However, during descent, the bottom part of SOTAB-I's body is directly against the water, while the movable wings are on the backside, minimizing the effect of heading control. In the case of heading control only during ascent, the robot drifted alongside the water current toward the north and west during descent in Figs. 3.45 and 3.46, respectively. In the case of

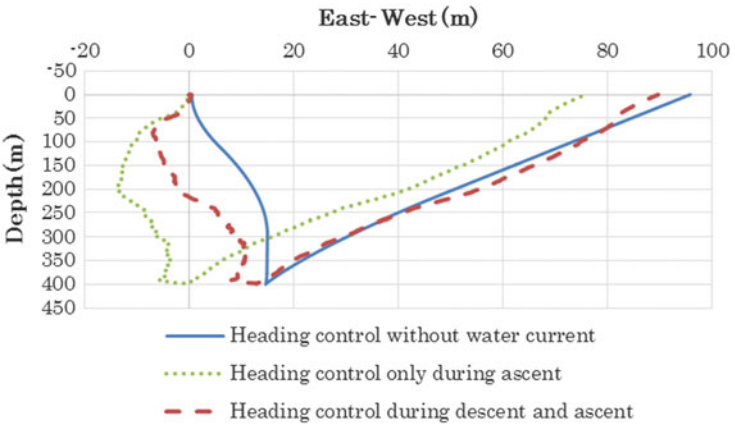

Fig. 3.45 Effect of water current on heading control in X–Z plane

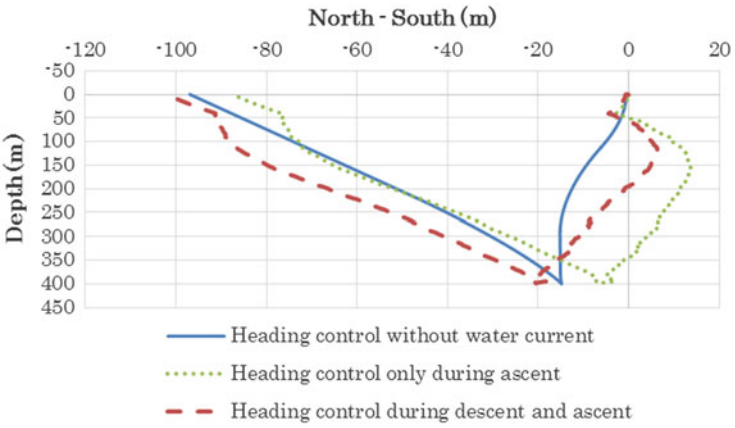

Fig. 3.46 Effect of water current on heading control in Y–Z plane

heading control during both descent and ascent, the effects of the water current on the horizontal displacement of SOTAB-I were both smaller in Figs. 3.45 and 3.46.

3.3.5.3 Simulation of Path Planning

In order to obtain the optimum results for spilled oil or methane plume surveying operation, SOTAB-I should go through these substances as much as possible. There are two main points influencing this eventuality: the trajectory of the robot coupled with spilled oil or methane plume movement in the ocean. Therefore, simulations of robot movement and spilled oil or methane plume behavior in the water (Kawahara et al. 2014) are needed. The results from both simulations will be combined to obtain

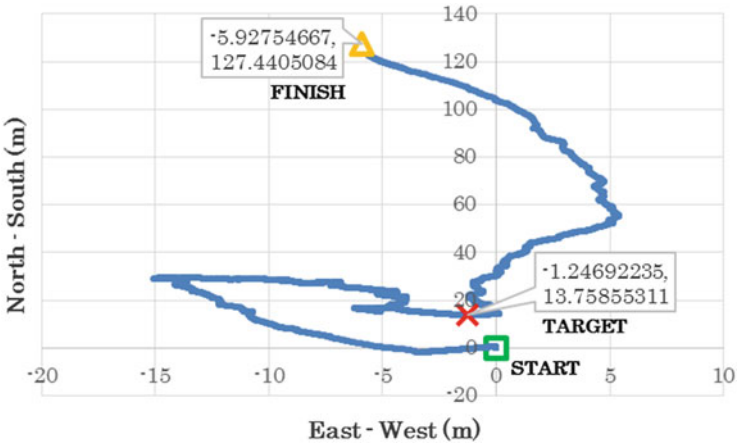

Fig. 3.47 Trajectory simulation in horizontal plane

the optimum path planning for SOTAB-I operation. Since the robot, spilled oil and methane plume movement are greatly affected by water current, it is important to obtain the vertical water current profile near the seepage point at first. This can be obtained through the initial surveying operation of SOTAB-I.

The best route for SOTAB-I in going through the spilled oil or methane plume will be determined from the simulations. After the best route for SOTAB-I is determined, the initial point for robot deployment can be obtained. This point will be used to guide the mother ship to locate the starting point for SOTAB-I deployment. From the X and Y displacements of SOTAB-I in Earth-fixed coordinates, the robot's trajectory in the horizontal plane can be acquired. While from the Z position in the Earth-fixed coordinates, the depth of SOTAB-I can be obtained.

Figure 3.47 shows the SOTAB-I trajectory simulation under the same water current conditions, as shown in Fig. 3.44. In this figure, the X and Y displacements of SOTAB-I are shown in the horizontal plane. The direction in which SOTAB-I will go under the effect of the water current can be observed from this figure. SOTAB-I starts its operation from the start point (0,0). Then, it would dive until reaching the target point. The target point is the position where the robot would reach the maximum depth. Then, it would start to ascend and resurface again at the finish point. The next step is to put the robot's trajectory onto the Earth's coordinate plane. If the target oil or methane gas seepage point is known, then the starting point where SOTAB-I should be deployed by the mother ship can also be obtained.

3.4 Water Surveying

3.4.1 Sensors Configuration and Calculation Process

3.4.1.1 CTD Data

Based on CTD measurements, it is possible to calculate the depth, salinity, density, and speed of sound. Table 3.5 summarizes oceanographic data that can be obtained with the CTD sensor with their associated symbols and scales.

Table 3.5 shows results for an example of data calculated based on CTD sensor measurements. The depth was calculated using the following formula:

$$\text{depth (m)} = \left(\left(\left(-1.82\text{P}^{*}10^{-15} + 2.279^{*}10^{-10}\right)\text{P} - 2.2512^{*}10^{-5}\right)\text{P} + 9.72659\right)\text{P}\big) / \text{g} \tag{3.8}$$

where P is the pressure in decibar and g is the local gravity value in m/s^2.

Formulas for the computation of salinity, density, and sound velocity were obtained from (Fofonoff and Millard 1983) after conversion of temperature from the international temperature scale ITS-90 to IPTS-68. Formulas for the computation of salinity, density, and sound velocity were obtained from (Fofonoff and Millard 1983).

Table 3.5 CTD-related oceanographic data

	Symbol	Unit	Comment
Temperature	T_{90}	[°C]	Given in ITS-90 scale
Conductivity	C	[S/m]	
Pressure	P	[dcb]	
Depth	D	[m]	
Salinity	S	[]	Given in practical salinity scale PSS-78
Density	ρ	[kg/m3]	Based on the equation of state for seawater – EOS80
Sound speed	V	[m/s]	Sound velocity is calculated based on Chen–Millero equation

3.4.1.2 Water Current Measurements

Introduction

Zhang and Willcox (1997) proposed a method to measure current velocities using an ADCP mounted on a cruising-type autonomous underwater vehicle (AUV) using a CTD sensor and a long baseline (LBL) acoustic navigation system. An et al. (2001) measured current velocities in shallow water using ADCP mounted on a small cruising-type AUV using a CTD sensor and an ultrashort baseline (USBL) acoustic navigation system. Stanway (2010) measured the current profile using ADCP/DVL mounted on a cruising-type AUV using a CTD sensor with bottom-lock DVL measurements. Medagoda et al. (2011) proposed an alternative approach to navigation for AUV in the mid-water column where GPS and DVL are not available by using ADCP and seafloor view-based simultaneous localization and mapping (SLAM). However, few references dealing with measurements of current profiles using ADCP and short baseline (SBL) or USBL in the mid-water column are available.

Absolute current velocity against the Earth in the mid-water column for the case of SOTAB-I equipped with ADCP/DVL, CTD, and USBL should be calculated by summing up the relative current velocity measured by ADCP on the vehicle and the speed of the vehicle, which is obtained by differentiating the position data obtained by USBL. The robot speed can also be measured directly using DVL within the device's range when it approaches the seabed. However, acoustic positioning is affected by multipath returns and circumferential noise. Thus, the accuracy of USBL data for obtaining its own speed becomes worse as depth and operation time increase. In fact, this phenomenon occurred in our experimental results. To obtain SOTAB-I's speed accurately, we propose an estimation method using ADCP and USBL. In Sect. 3.4.3, vertical water column survey part, the water column current profile at a water depth of 50 m off Komatsushima by this method was evaluated by comparing with that by the method using DVL and ADCP and that by the method using ADCP of the mother ship. The water column current profile between water depths of 15 and 50 m at depth to the bottom at 700 m at Toyama Bay by this method was also evaluated and compared with that by the method using the ADCP of the mother ship. Definitions of symbols corresponding to sensor data are shown in Table 3.6.

Table 3.6 Definitions of symbols

Symbol	Definition	Sensor
$\boldsymbol{V}_c$ ($\boldsymbol{V}_{cx}$, $\boldsymbol{V}_{cy}$, $\boldsymbol{V}_{cz}$)	Relative current velocity and components	ADCP
$\boldsymbol{V}_s$ ($\boldsymbol{V}_{sx}$, $\boldsymbol{V}_{sy}$, $\boldsymbol{V}_{sz}$)	Robot speed and components	DVL
$\boldsymbol{X}_s$, $\boldsymbol{Y}_s$, $\boldsymbol{Z}_s$	Robot position	USBL
$\boldsymbol{Z}$	Depth position of robot	CTD
$\boldsymbol{\theta}$, φ, $\boldsymbol{\psi}$	Pitch, roll, and yaw angles of the robot	ADCP, azimuth, compass

USBL Characteristics

USBL is an underwater direction and distance detection device using a broadband acoustic spread spectrum signal processing system. The transceiver on the mother ship sends a signal and the transponder attached on the top of the robot replies. The distance between the mother ship and the robot is determined by the round-trip time of sound waves and water speed, and the angle is calculated from the phase difference at the reception arrays of the USBL. Then, the relative position of the transponder against the transceiver in three-dimensional space can be calculated. USBL is also used to determine the position of the diver and installation object in the water. There are several kinds of transceiver depending on the length of acoustic communication. Our robot has adopted the transceiver called TrackLink 5000/TC5000HA. The characteristics of this transceiver are shown in Table 3.7.

The frequency zone used in acoustic positioning is between 100 Hz and 1 MHz depending on the objective. Robots, which are assumed to be used in deep water such as our robot, use a transceiver operating at a relatively low frequency. The beam width is within 120°. If the transponder gets out of place in this range, communication accuracy will become significantly worse or it will lose communication itself. An image of the position between the transceiver installed on the mother ship and the transponder installed on our robot is shown in Fig. 3.48. The transceiver on the mother ship is installed less than 3 m from the sea surface. From the characteristics of the beam width, the mother ship must be operated to keep the horizontal distance between the robot and the mother ship $\sqrt{3}$ times less than the distance of the depth of SOTAB-I. However, near the sea surface, it should keep its distance because there is a risk of collision with the mother ship if they are close to each other. For this reason, accuracy of positioning data measured by USBL is worse near the sea surface. Figure 3.49 shows a comparison of measured depths obtained by CTD and USBL. The depth data measured by USBL between 0 and 50 m has noise. When we produce water column profiles, we adopt the depth data measured by CTD as the depth of the robot because CTD has high accuracy compared with the accuracy of the USBL positioning data (see Fig. 3.49).

Table 3.7 Characteristics of the transceiver in SOTAB-I

Characteristics of the transceiver (TrackLink5000/TC5000HA)	
Positional accuracy	0.15°
Measurement distance	5000 m
Beam width	120°
Target point	8 point
Frequency used	14.2–19.8 kHz
Water depth of the pressure resistance	20 m
Dimension	26 cm × 12.6–16.0 cm (diameter)
Weight	5.2 kg
Weight in water	2.3 kg

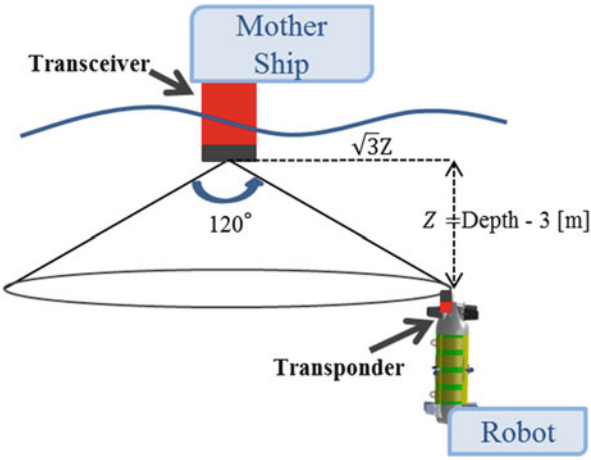

Fig. 3.48 Schematic view of the relationship between the position of the transceiver installed on the mother ship and the transponder installed on the robot

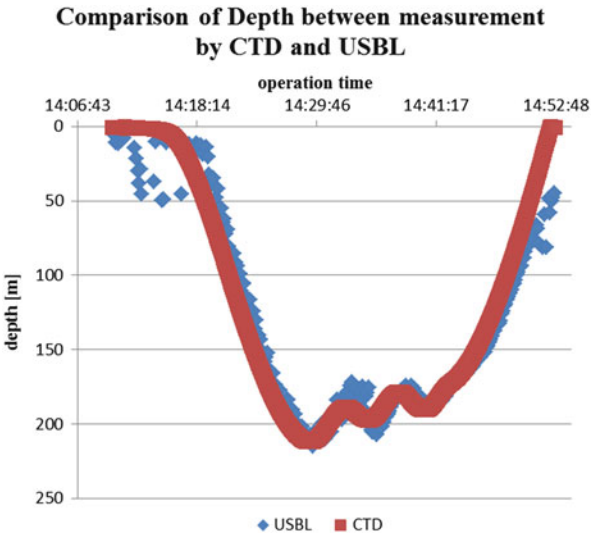

Fig. 3.49 Comparison of depths measured by CTD and USBL

ADCP Characteristics

The robot processor connects to the ADCP/DVL device through an RS232 serial port. The selected output format is PD0, which is a binary format that provides the greatest possible information. A virtual serial splitter serves to duplicate the serial data output. One is directed to serial logger software to save data in a file for later detailed analysis. The other is input to the main program for real-time processing of water currents and bottom tracking data.

The SOTAB-I configuration was set as water profiling done every second for 10 water layers and referred to also as bins with 0.5 m thickness. Measurements are configured to be given in Earth coordinates, taking into consideration tilting and bin

Table 3.8 SOTAB-I ADCP configuration

ADCP configuration	Symbol	Value
Sampling time	TE	1 s
Pings/ensemble	WP	1
Number of depth cells	WN	10
Layer thickness	WS	0.5 m
Water profiling mode	WM	1
Blank after transmit	WF	0.44 m
Salinity	ES	35
Depth of transducer	ED	0 m
1st Bin distance		0.99 m
Coordinate transformation	EX	0 × 1 F (Earth coordinates, use tilts, 3-beam solutions, bin mapping)

mapping. The most important characteristics and configuration are summarized in Table 3.8.

The ADCP is installed in the top bottom of the body. Water current data are collected when the robot is descending to reduce the turbulence that is induced by robot body motion.

Water Column Regions

The water vertical column is divided into three zones: near-surface zone, middle zone, and near-seabed zone, as shown in Fig. 3.50. The absolute water current velocity denoted as V is the sum of the absolute velocity of the robot denoted as V_s and the relative water current velocity against the robot denoted as V_c, as expressed in the following equation:

$$V = V_c + V_s \tag{3.9}$$

In the near-surface zone between 0 and 20 m of water depth, the most effective way to obtain V is to use the ADCP on the mother ship. As previously explained, the transceiver has the limit of the beam width for acoustic communication. In this zone, the horizontal distance from the mother ship to SOTAB-I is likely to become long compared with its depth. Therefore, we cannot obtain highly reliable speed data by differentiating the USBL position data. Instead, we can know those data from the ADCP on the mother ship, which can measure water currents accurately within the water depth to 100 m.

In the middle zone, the only method to estimate V_s is to differentiate the position data measured by USBL. However, the accuracy of USBL data for getting its own speed becomes worse as the water depth increases and as operational time becomes longer. In fact, these phenomena occurred in our experimental results.

In the near-seabed zone, SOTAB-I, equipped with an ADCP and a DVL, can measure both the relative current velocity and its own speed against the Earth

Fig. 3.50 Water layers for estimation of water current

directly. Then we can obtain absolute water currents. DVL also outputs the altitude from the seabed from 30 to 0 m.

Near-Seabed Zone

The ADCP is installed at the bottom of the robot. Water current data are collected when the robot is descending or ascending. The data during descending, however, are analyzed to reduce the influence of turbulence, which is dominantly generated in the wake region behind the fuselage of the robot during ascending. As mentioned, in this zone, the robot speed V_s can be measured by DVL, which measures the robot speed against the seabed. Thus, the relative water current velocity measured by the ADCP is the value with respect to robot-fixed coordinates (X, Y, Z). Therefore, it needs to be transformed to Earth-fixed coordinates (X_E, Y_E, Z_E). Figure 3.51 shows the relationship between robot-fixed coordinates and Earth-fixed coordinates. If we suppose V (V_X, V_Y, V_Z) as the robot speed against SOTAB-I, V_s in Earth-fixed coordinates is written as (3.10), then the absolute water current velocity can be obtained by (3.9).

$$V_s = \begin{pmatrix} V_{sx} \\ V_{sy} \\ V_{sz} \end{pmatrix} = T^{-1} \begin{pmatrix} V_X \\ V_Y \\ V_Z \end{pmatrix} \tag{3.10}$$

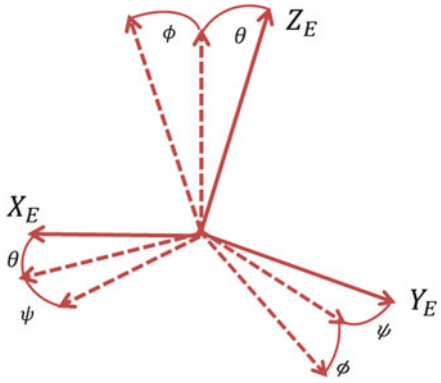

Fig. 3.51 Transformation to Earth-fixed coordinates

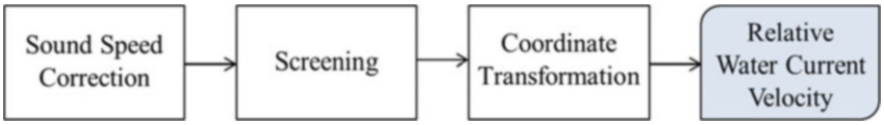

Fig. 3.52 The process of calculating relative water current velocity from ADCP

$$T = \begin{pmatrix} \cos\theta\cos\psi & \cos\theta\sin\psi & -\sin\theta \\ \cos\psi\sin\phi\sin\theta - \sin\psi\cos\phi & \sin\psi\sin\phi\sin\theta + \cos\psi\cos\phi & \sin\phi\cos\theta \\ \cos\psi\cos\phi\sin\theta + \sin\psi\sin\phi & \sin\psi\cos\phi\sin\theta - \cos\psi\sin\phi & \cos\theta\cos\phi \end{pmatrix} \tag{3.11}$$

The process of calculating relative water current velocity V_c is shown in Fig. 3.52.

The ADCP calculates the component of relative flow velocity V (m/s) for each depth cell using equation (3.12):

$$V = F_D \frac{C}{2Fs}, \tag{3.12}$$

where F_D is the measured Doppler frequency shift in the direction of each acoustic beam, C is the speed of sound in water at the transducer face in m/s, and F_S is the transmitted acoustic frequency.

From the equation, the accuracy of velocities in any coordinate system is directly connected to the sound speed: an error of 1 % in sound speed will result in 1 % error in velocity measurement. The sound speed in seawater depends on pressure, temperature, and salinity. The WHN120 integrates a thermistor to measure temperature, but it is not equipped with any pressure or salinity sensors. The ADCP calculates sound speed based on the measured temperature and preset salinity. However, the salinity of seawater is variable, especially near the sea surface. To obtain accurate velocity data, the ADCP needs to know the real speed of sound in water. For that reason, sound speed near the transducer is calculated based on the CTD sensor measurements.

It is possible to correct the velocity data in post-processing by using the following Eq. 3.13:

$$V_{\text{CORRECTED}} = V_{\text{UNCORRECTED}} \ (C_{\text{REAL}}/C_{\text{ADCP}}) \,, \tag{3.13}$$

where C_{REAL} is the real sound speed at the transducer and C_{ADCP} is the sound speed used by the ADCP.

Ranges of cells, to a smaller extent, are also affected by sound speed variations and then are subject to correction. Range may be corrected by using the following equation:

$$\text{L}_{\text{CORRECTED}} = \text{L}_{\text{UNCORRECTED}} \, (C_{\text{REAL}}/C_{\text{ADCP}}) \,, \tag{3.14}$$

where

$\text{L}_{\text{CORRECTED}}$: Corrected range cell location
$\text{L}_{\text{UNCORRECTED}}$: Uncorrected range cell location

Screening is performed automatically by the ADCP. Velocity data are subject to four kinds of screening: the correlation test, the fish-rejection algorithm, the error-velocity test, and the percent-good test. At this stage, the ADCP checks the reasonableness of the velocity components for each depth cell and flags bad data. Then, the Euler transformation must be performed using the same method as for calculating the robot speed from the DVL data (see Fig. 3.52).

Middle Zone

The ADCP data in the middle zone are treated in the same way as described above. To obtain accurate SOTAB-I speed, we suggest an estimation method using USBL positioning data.

The raw USBL data are output as a geographic coordinate system. First, we convert them to a rectangular coordinate system to differentiate position data and obtain the velocity.

Second, the distance-based outlier method (DB method) is used to remove outliers because jumping and shifting sometimes happen to the USBL position data. The DB method is an outlier method based on the distance SOTAB-I moves. It regards points as outliers if the measured values cannot be realistically achieved. The robot speed in the horizontal direction is considered to be smaller than 0.5 m/s because of its characteristic that the moving speed is not much different from the water current velocity in the horizontal direction. If the acoustic communication status between SOTAB-I and the mother ship is normal, the reception interval is every 7 or 8 s and the distance moved during that time is 4.0 m at a maximum. Then, for each measured point, we calculate the horizontal distances $R_i - 3 \sim i + 3$ between the corresponding point and each of the three previous points and the three succeeding points, as shown in Eq. 3.15. If there are more than five points within the circle with a radius of R equal to 12 m as shown in

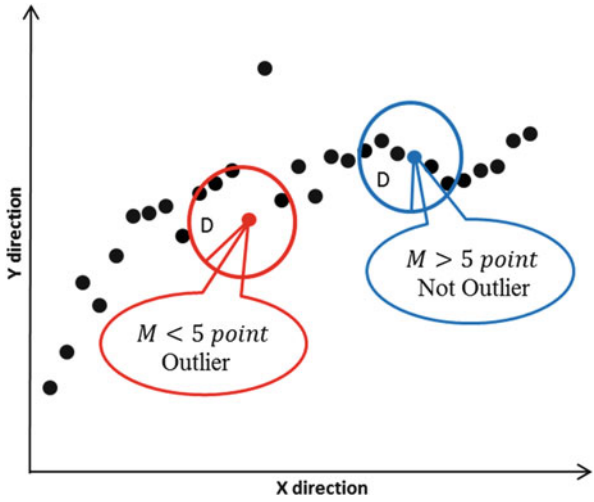

Fig. 3.53 Schematic view of the DB outlier method

Eq. 3.16, the point is determined not to be an outlier, otherwise, it is judged as an outlier. Figure 3.53 shows a schematic view of the DB outlier method.

$$R_{i-3\sim i+3} = \sqrt{(X_{i-3\sim i+3} - X_i)^2 + (Y_{i-3\sim i+3} - Y_i)^2} \tag{3.15}$$

$$R = 0.5\,[m/s] \times 8\,[s] \times 3 = 12\,[m] \tag{3.16}$$

The X, Y, and Z positioning data measured by the USBL have a correlation with the timing when the error value is generated. When one of these values is judged as an outlier, all of those are judged as outliers. An example of the effect of the DB method applied to experimental USBL data is shown in Fig. 3.54. The upper figure shows the trajectory in the east–west direction of SOTAB-I measured by USBL. The lower figure shows the trajectory in the north–south direction.

SOTAB-I usually receives USBL positioning data every 7 or 8 s by acoustic communication. However, it sometimes fails to receive data and the time interval becomes long. This phenomenon causes mistakes in the judgment in the application of the DB method, even though they are not outliers. This is the reason why we apply linear interpolation to the positioning data before treating with the DB method. Then the SOTAB-I speed can be obtained by differentiating these position data shown as Eq. 3.17:

$$\frac{X_n - X_{n-1}}{\delta t} = V_{n-1} \tag{3.17}$$

In addition, we treat one more type of outlier. Outliers are checked by whether the calculated velocity data are within $\mu \pm 3\sigma$, where μ and σ are given by:

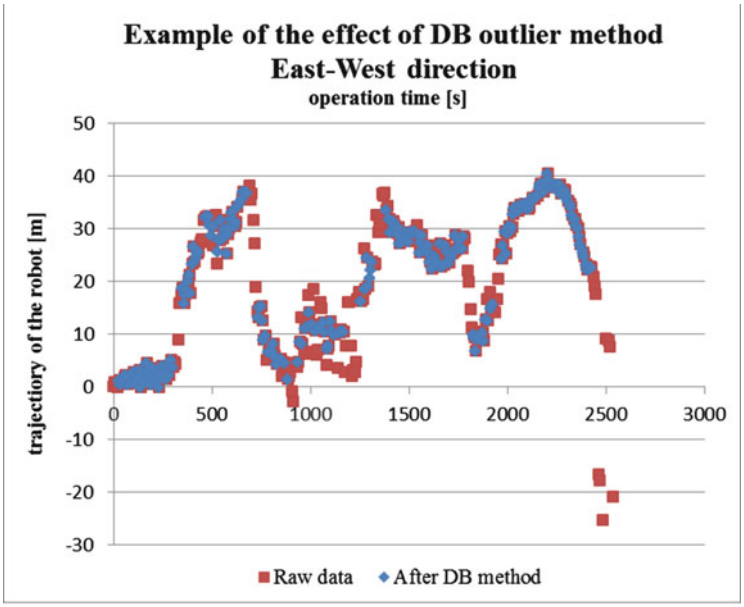

(a) An example of the effect of the DB method in east-west direction

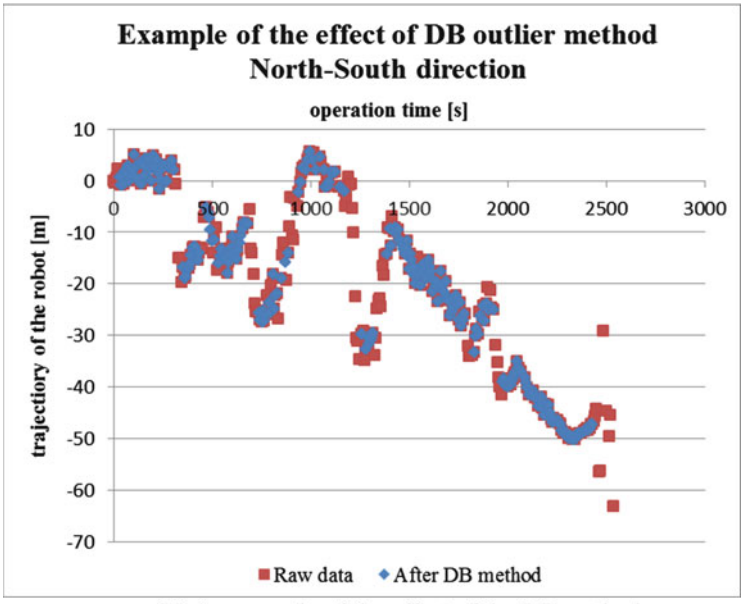

(b) An example of the effect of the DB method in north-south direction

Fig. 3.54 An example of the effect of the DB method (**a**) in east–west direction (**b**) in north–south direction

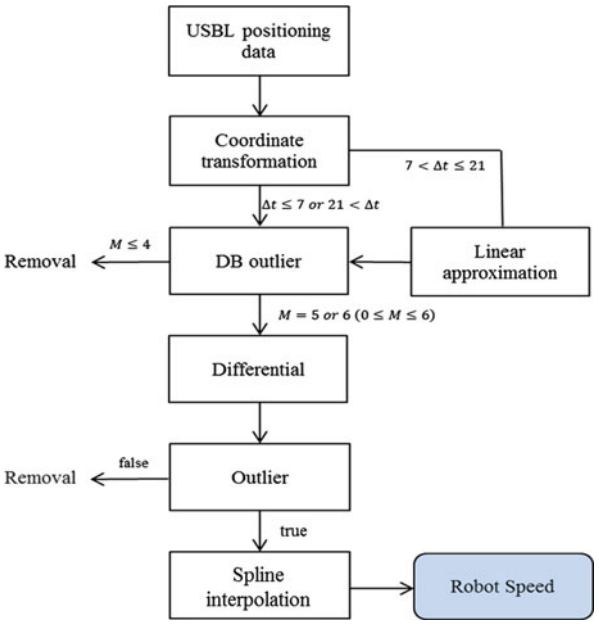

Fig. 3.55 Overview of the system diagram to estimate SOTAB-I speed from USBL

$$\mu = \frac{1}{N}\left(\sum_{i=1}^{N} V_i\right) /N, \tag{3.18}$$

$$\sigma^2 = \frac{1}{N}\sum_{i=1}^{N}(V_i - \mu)^2 . \tag{3.19}$$

N,V_i,μ, and σ denote the number of those data, data value, the average value, and standard deviation, respectively.

Finally, we use spline interpolation and get the absolute robot speed V_s. An overview of the system diagram to estimate SOTAB-I speed is shown in Fig. 3.55.

3.4.1.3 Dissolution of Substances

The UMS was calibrated for dissolved gases (methane, nitrogen, oxygen, argon, and carbon dioxide) by equilibrating acidified artificial seawater for more than 1 h with gas mixtures that contained certified mole fractions of the gases. Salinity and temperature, measured during sample analysis, allowed calculation of dissolved gas concentrations. Gas volume percentages are shown in the UMS that was calibrated for ethane, propane, and butane by equilibrating seawater with gas mixtures that contained a certified mole fraction of ethane, propane, or butane for two-point calibrations of these gases (background and one concentration). The UMS was also calibrated for VOCs by analysis of VOC standards created by serial dilution of stock solutions of benzene, toluene, and xylenes. Calibration was not performed

for hydrogen sulfide or naphthalene. Each sample was analyzed until a stable signal was achieved. Blank samples (i.e., UMS residual gas backgrounds) were measured by leaving deionized water in the MIMS assembly with the sample pump inactivated overnight to allow complete degassing of the sample in contact with the membrane. The UMS assembly temperature was controlled at 25 °C during calibration to mimic deployment conditions. The UMS cast data were subsequently converted to concentrations for the dissolved gases (μmol/kg) and VOCs (ppb) from the calibration parameters and concurrently collected physical (CTD) data using algorithms and software developed by SRI International (Table 3.9).

Linear least-squares regressions provided UMS calibration coefficients for methane, nitrogen, ethane, oxygen, propane, argon, carbon dioxide, and butane concentrations using measured UMS ion currents, at m/z of 15, 28, 30, 32, 39, 40, 44, and 58. The ion current at m/z 44 (called I44), which is the mass spectrometer ion signal intensity for m/z 44 corresponding to the diagnostic ion for carbon dioxide, was also used in the nitrogen regression to account for contributions from carbon dioxide fragmentation.

Additionally, all signal intensities were background corrected by subtracting the signal intensity at m/z 5 (electronic background); this subtraction accounts for changes in electronic noise resulting from UMS temperature variability. The signal intensity at m/z 5 is used as the electronic background because there is no chemical that will give a peak in the mass spectrum at m/z 5. The "argon" or "water" correction is then used, as described in literature (Bell et al. 2007; Bell 2009), to account for temperature variations in the field. The UMS calibration parameters and deployment parameters were identical. The calibration parameters that were identical were the sample flow rate and temperature of the membrane introduction heater block. A time delay was applied to the UMS cast data to adjust for the sample travel time through the tubing and membrane permeation.

The argon and water vertical profiles are the measured ion intensities at m/z 40 (argon) and m/z 18 (water vapor) as a function of depth. These are used to

Table 3.9 Standard gas mixtures used for equilibration (in volume %)

Gas	Mixture 1	Mixture 2	Mixture 3	Mixture 4
Methane	0.0995	0.2500	2.5000	3.351
Nitrogen	Balance	Balance	Balance	Balance
Oxygen	20.85	21.0000	17.0100	9.9600
Argon	1.009	1.3010	1.0040	0.6990
Carbon dioxide	0.0990	0.7510	0.1500	0.0400

Gas	Mixture 5	Mixture 6	Mixture 7
Nitrogen	Balance	Balance	Balance
Ethane	0.1000		
Propane		0.1000	
Butane			0.1000

normalize the concentration profiles of the other analyses to account for changes in permeation through the membrane interface with increased pressure, as well as other changing environmental conditions that affect the signal intensities (Bell et al. 2007; Bell 2009; Bell et al. 2011). Therefore, high-frequency noise in these data sets was removed using a Butterworth filter prior to normalization of the other profiles.

The typical measurement accuracy at best is 2 %, but this varies for different chemicals. The response time is at best 5–10 s for the light compounds and worse for the high molecular weight compounds. A typically reasonable spatial resolution can be obtained with an ascent and descent rate of 0.5 m/s. As mentioned in the robot maneuverability section, the maximum vertical and lateral speed of the SOTAB-I are below that rate.

3.4.2 Vertical Water Column Survey in the Gulf of Mexico

At-sea experiments were performed from the 6th to the 15th of December 2013 in the Gulf of Mexico in the USA (Fig. 3.56), near where the Deepwater Horizon oil spill accident in 2010 and the Hercules 265 oil rig blowout in 2013 occurred that led to the release of methane gas. The aim of the exploration was the evaluation of the performance of the SOTAB-I's surveying abilities (Choyekh et al. 2014). Due to the strong wind and severe weather conditions, experiments were carried out in shallow water and in particular at the mouth of the Mississippi River, where the UMS data were measured. The area is characterized by its prevalent abandoned oil rigs and natural seepage of hydrocarbons (Mitchell et al. 1999).

This section is mainly focused on the experimental results obtained on the 13th of December 2013 from 13:30 to 14:30 dive.

Figure 3.57 displays the meteorological data reported by the PSTL1 station on the 13th of December 2013. The station is located in the mouth of the Mississippi River at the position (28°55′56″ N 89°24′25″ W). The distance between the PSTL1 station and the place where the experiments were carried out on the 13th of December 2013 is around 20 km. The station reported a southeastern wind direction with a gradually decreasing speed from 5 m/s at the time of the experiment. Water temperature was 13 °C, and atmospheric temperature was 20 °C.

3.4.2.1 Temperature, Salinity, and Density

Figure 3.58 displays the vertical distributions of temperature and salinity measured by the CTD. It can be observed that the sea temperature in the upper layer is colder than in the bottom layer (Fig. 3.58a), which can be explained by the cold atmospheric temperatures that dropped under 12 °C on the day that preceded the experiments. The atmospheric temperature reported by the PSTL1 buoy database was between 13 and 19 °C at the time of the experiments on the 13th of December (Fig. 3.57). The salinity level near the sea surface changed

Fig. 3.56 Gulf of Mexico experimental zone (Google Map)

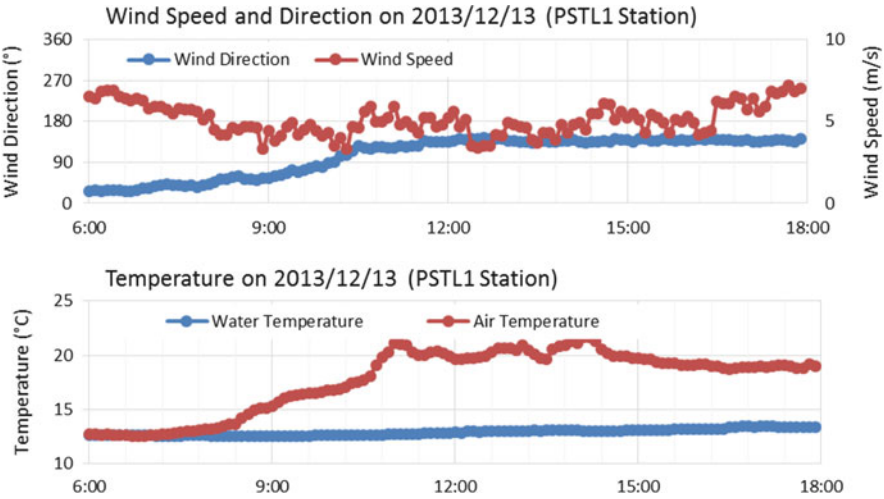

Fig. 3.57 Air and sea temperature and wind speed reported by the PSTL1 station on the 13th of December 2013

considerably from 28 ppm at 2 m water depth to 34 ppm at 8 m (Fig. 3.58b),. This can be explained by the location of the site, which is in the middle of the Mississippi mouth where freshwater flows out to the Gulf of Mexico. The freshwater layer was breached through an adjustment of the buoyancy device. The density depends on temperature, salinity, and pressure. In Fig. 3.58c, it can be observed

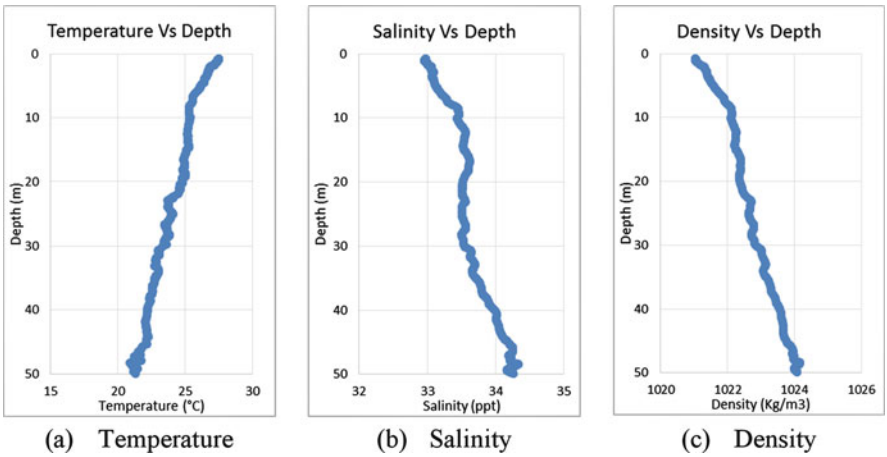

Fig. 3.58 Vertical distributions of temperature and salinity measured by the CTD: (**a**) temperature, (**b**) salinity, and (**c**) density

that the increase of density was primarily dominated by the large variation of salinity.

3.4.2.2 Water Currents

In the Gulf of Mexico experiments, the VRU was not installed, which led to less accurate positioning values due to the effect of ship tilting. For that reason, vertical water currents were only measured when the robot was within bottom track range. In this experiment, the number of layers of the ADCP was set to five layers with 0.5 m thickness. The water column profiling was based on the measurements obtained from the first layer. Figure 3.59 illustrates that the current magnitude becomes stronger in the east–west direction as the robot approaches the seabed. Water current flowed mostly in the eastern direction.

3.4.2.3 Dissolution of Substances

Figure 3.60 illustrates the change of concentration of some substances along the water column. Figure 3.60a, b shows the respective vertical concentration profiles for nitrogen and argon needed for the calculation of the other substances' dissolution profiles mentioned previously. Figure 3.60e demonstrates that the concentration of methane in the upper water layers is negligible down to a depth of 30 m, and it starts to increase steadily down to a water depth of 44.6 m. In Fig. 3.60d, it can be observed that the oxygen concentration moderately decreased from a water depth of 0 m to that of 10 m, followed by a slower rate of decline from 10 to 27 m water

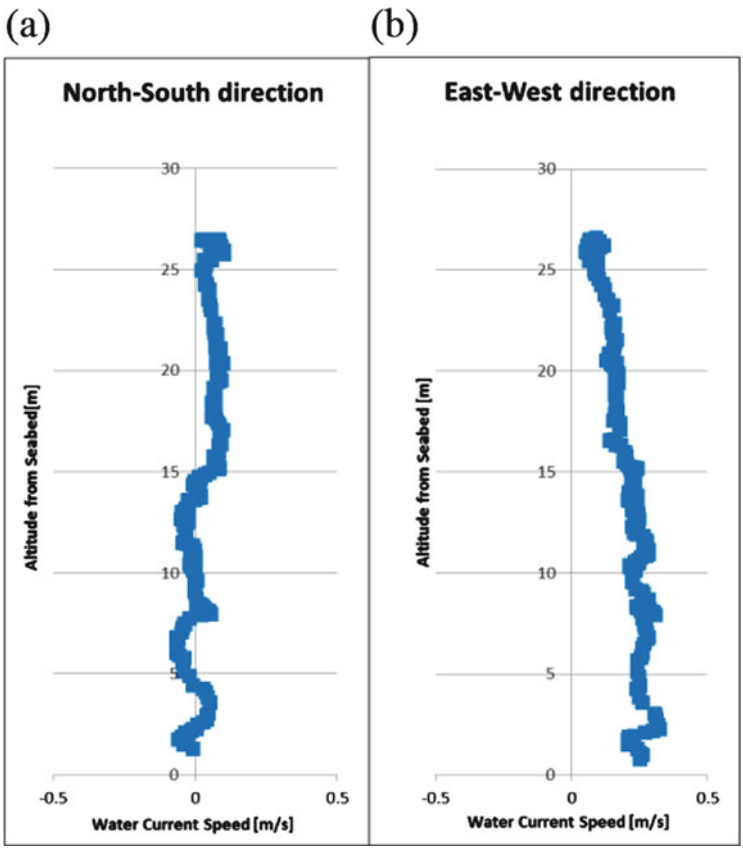

Fig. 3.59 Vertical profile of water currents (**a**) in north–south direction, and (**b**) in east–west direction

depth. Then, oxygen concentrations declined considerably from a water depth of 27 m to that of 44 m. It can be seen that the oxygen concentration decreased with increasing depth. In Fig. 3.60c, three zones can be distinguished based on the change in carbon dioxide concentrations: in water depths between 0 and 10 m, carbon dioxide concentrations decreased gradually. From 10 to 27 m, it kept decreasing, but at a slower rate. Below 30 m, carbon dioxide concentrations increased down to a water depth of 44 m.

From this perspective, we can say that the SOTAB-I succeeded in measuring dissolved substance variations along the vertical water column. Conversely, other alkanes and benzene-toluene-xylene (BTX) were below the sensory threshold and had no significant concentrations.

Very few methods will verify or corroborate the UMS measurements. We have used dissolved oxygen (DO) sensors in the past to compare the UMS oxygen measurements (m/z 32), and the comparison was generally very good (Bell et al.

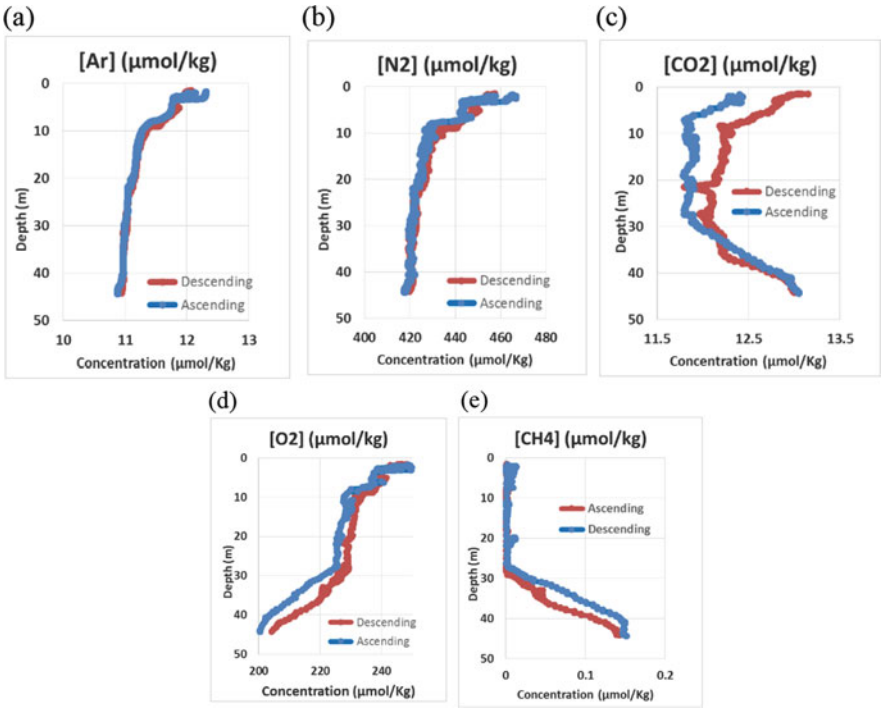

Fig. 3.60 Dissolution of substances in the water column: (**a**) methane (**b**) oxygen (**c**) carbon dioxide (**d**) nitrogen (**e**) argon

2007; Bell 2009). The SOTAB-1 deployments were not in a location where we would expect to see alkanes and BTX. We believe that the methane that we detected was biogenic methane and not associated with an oil reservoir. We have verified the UMS ability to detect these compounds in the lab and in other deployments (see Wenner et al. 2004 for BTX using an earlier version).

3.4.3 Vertical Water Column Survey in Komatsushima

Sea experiments in the shallow water region were carried out off Komatsushima, Japan (33° 96′ N, 134° 82′ E), on the 24th and 25th of July 2014, as shown in Fig. 3.61. The mother ship employed in the experiments was the "Fukae-maru" of Kobe University. The ship length is 49.97 m and its breadth is 10 m. The ship has an ADCP for measuring water currents. The water depth where the experiments took place was around 50 m.

Fig. 3.61 Pictures of the sea experiments and the location off Komatsushima

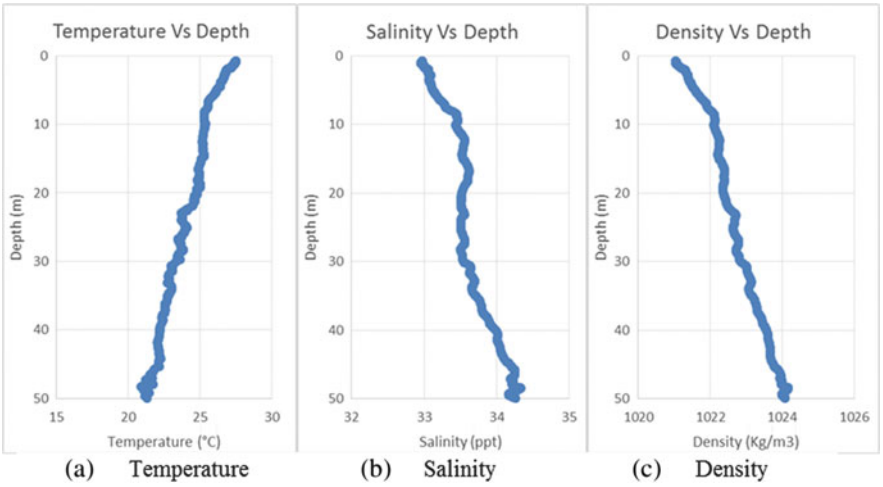

Fig. 3.62 Water column distribution of temperature, salinity, and density

3.4.3.1 Vertical Distributions of Temperature, Salinity, and Density

Figure 3.62 shows an example of data calculated based on CTD sensor measurements. As depth increases, temperature becomes lower, and salinity and density become higher.

3.4.3.2 Comparison of Vertical Water Currents Profile

We can obtain water currents at the same time and the same sea area in three ways. One is using the ADCP installed on the "Fukae-maru" and its speed. The second is using the ADCP and USBL installed on SOTAB-I. The third is using the ADCP

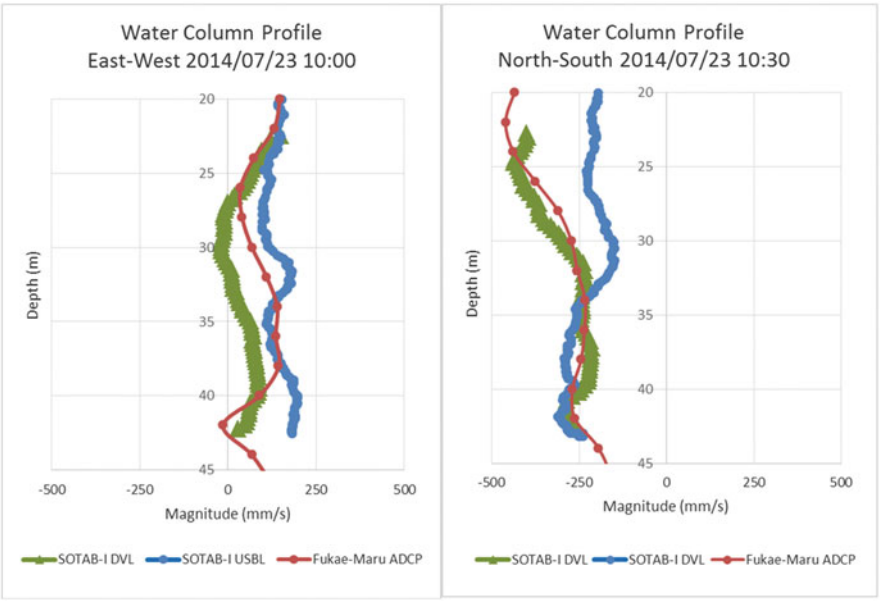

Fig. 3.63 Comparison of water current profiles measured by the three methods

and DVL installed on SOTAB-I. Figure 3.63 shows a comparison of water current profiles obtained using these methods. The profiles measured by the "Fukae-maru" are plotted along the vertical line at intervals of 3 m at a certain time. The ship drifted about 200 m from 9:50 to 10:00 while SOTAB-I was diving. Therefore, there are spatial and temporal differences of water currents between estimations and measurement by the mother ship. The results of measurements by the mother ship show almost the same curve trend regardless of a small difference in time and position. Comparison of the water current profile between estimation using DVL and measurement by the mother ship shows that the vertical profile of the water current direction is very similar, particularly in both directions. The estimation using USBL was not successful because the data measured by USBL included a lot of noise and shift in the shallow water region from 0 to 15 m as we mentioned. Comparison of the water current profile between USBL estimation and measurement by the mother ship shows that the vertical profile of the water current direction using USBL agrees well with that using the mother ship in both directions. However, the speeds are different and the maximum difference is around 0.2 m/s.

Fig. 3.64 Pictures of the sea experiments and location in Toyama Bay

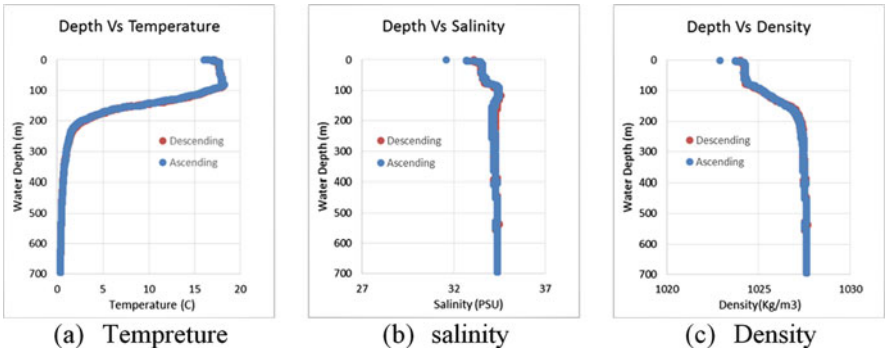

Fig. 3.65 Vertical distributions of temperature and salinity measured by the CTD: **a** temperature, **b** salinity, and **c** density

3.4.4 Vertical Water Column Survey in Toyama Bay

We conducted experiments at Toyama Bay, Japan (36° 52′ N, 137° 09′ E), twice, as shown in Fig. 3.64. The water depth where these experiments took place was around 700 m. One was carried out on the 29th and 30th of July 2014 and SOTAB-I dove to around 50 m. It indicates that DVL did not work in this region because the target depth was out of the device's range. The other was carried out on the 27th and 28th of November and SOTAB-I dove to around 700 m.

3.4.4.1 Temperature, Salinity, and Density

Figure 3.65a shows seawater temperature distribution along the water column. Three zones can be distinguished. The first, which is called "mixed layer," is very dependent on the atmospheric temperature. In the experiments day, atmospheric temperature was colder than the sea surface temperature. Seawater temperature increased with depth at a fast rate on the first 10 m, followed by a slow rate up

to 90 m. In the second zone, called the thermocline zone, a sharp decrease of seawater temperature from 18 to 2° can be observed between 90 and 200 m water depth. The last zone – the deep layer – is the coldest layer and features a slow rate temperature change. The temperature reached 0.35° near 700 m water depth. The salinity profile (Fig. 3.65b) can also be divided into three distinct zones. In the surface zone, a sharp variation of salinity in the upper 10 m layer can be observed. It is due to the precipitations that preceded the experiments and to the nature of the bay, which is surrounded by the Northern Japanese Alps characterized by high mountain ranges and multiple rivers, a source of freshwater. The second zone is the halocline zone. It is characterized by a sharp increase in the salinity level up to 34.5 practical salinity units (psu) from 70 to 100 m depth. Finally, in the deep zone, a slight decrease of 34.2 psu occurred at 150 m depth, followed by a slow increase till 34.4 psu at 700 m water depth. Based on the temperature and salinity profiles, the vertical column density distribution could be obtained (Fig. 3.65c). It can be divided into three layers. In the mixed layer, low salinity water coming from rain and fresh river water is mixed with the seawater. In this layer, the density trend is more dominated by salinity variation. The second zone, called the pycnocline layer, can be distinguished between 70 and 170 m, where seawater density varies rapidly from 1,024.3 to 1,027.2 kg/m^3; it is explained by the fast increase of the salinity in the halocline zone between 70 and 100 m and then the rapid decrease of sea temperature in the thermocline zone between 90 and 200 m water depth. Finally, in the deep layer, a slow rate increase of density is observed. Density measured near 700 m water depth was equal to 1,027.6 kg/m^3. It can be noticed that the vertical water distributions of the temperature, the salinity, and the density are very similar in ascending and descending conditions. Slight differences are due to the temporal and spatial conditions in addition to the slight variance of the accuracy of the CTD sensor with its environmental temperature.

3.4.4.2 Vertical Profile of Water Currents

In the experiment on the 29th and 30th of July 2014, water currents could be obtained in two ways, estimation using USBL and ADCP measured by SOTAB-I and measurement by the mother ship "Wakashio-maru" equipped with ADCP. The length of the "Wakashio-maru" of the National Institute of Technology, Toyama College, is 53.59 m and its breadth is 10.00 m.

Figure 3.66 shows a comparison of water current profiles between these methods. The profiles measured by the "Wakashio-maru" are plotted along the vertical line at intervals of 8 m. The ship drifted around 100 m, while SOTAB-I was diving from 13:15 to 13:30. Therefore, time and position are a bit different, as in the case of the Komatsushima experiments. According to the results of the mother ship, they are almost the same curve trend regardless of time and position. The results of measurement by the mother ship show almost the same curve trend regardless of a small difference in time and position. Comparison of water current profile between estimation using USBL and ADCP of SOTAB-I and measurement by the

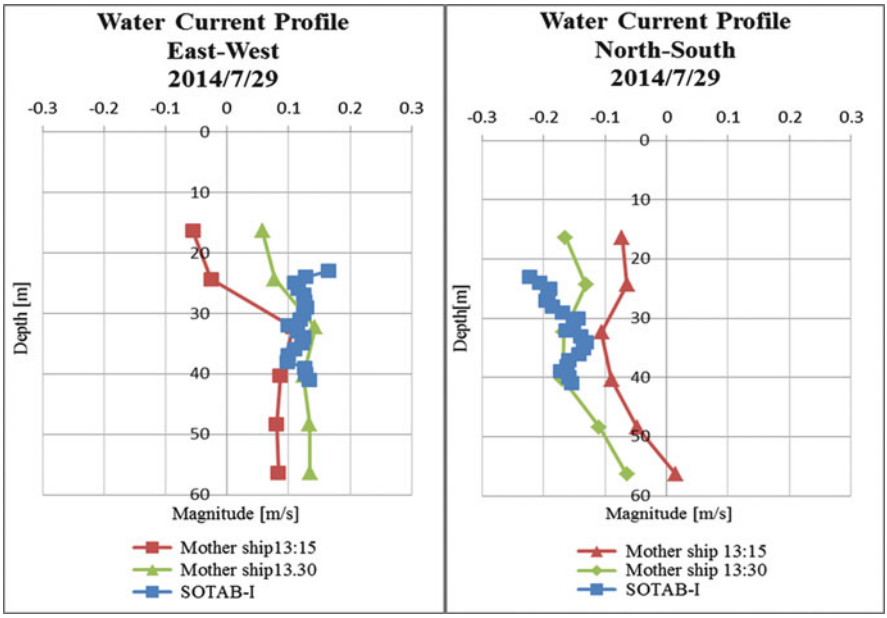

Fig. 3.66 Comparison of water current profile between estimations and measurement by the mother ship at Toyama Bay

mother ship shows that not only directions but also speeds of vertical profile of water current estimation using USBL and ADCP of SOTAB-I agree well with that using the mother ship in both directions.

The water current profile down to 700 m water depth in the experiment on the 27th and 28th of November is shown in Fig. 3.67. We used "Sazanami" as the mother ship. It is much smaller than the "Wakashio-maru" and is not equipped with ADCP. Therefore, the water current profile could not be evaluated by comparing other methods, especially the increase of the velocity from 500 m water depth in north–south direction.

3.5 Conclusions

To prevent further damage caused by oil spills and gas blowout accidents, a spilled oil and gas tracking autonomous buoy system (SOTAB-I) was developed. It has the advantages of being a compact system with extended surveying range. The robot can perform on-site measurements of several chemical substances dissolved simultaneously and is able to collect oceanographic data. The SOTAB-I can transmit data in real time with their corresponding position, making it very suitable for rapid inspection. Data collected will be processed by simulating and predicting programs

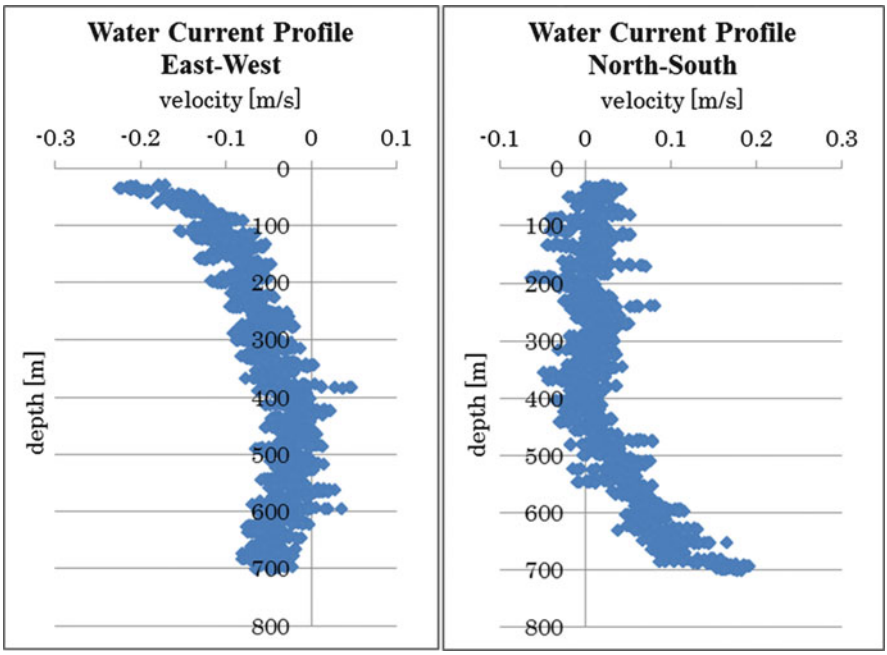

Fig. 3.67 Water current profile in deep water at Toyama Bay

that will help to explain the environmental changes due to the accident and boost the accuracy of oil drifting simulation. Consequently, establishing a better deployment strategy of collecting data becomes possible and will contribute to the efforts to avoid further damage that can be caused by oil spill disasters.

The outline of SOTAB-I and its general characteristics were described in this chapter. A summary of the main features of its internal devices was given. The SOTAB-I software design and organization were presented and an overview of its GUI was given. On the ship side, a GUI was designed, and it is a valuable tool to keep the user informed about the status of the robot and the changes around its environment. Additionally, it allows sending of commands when necessary. From the robot side, the multilayered architecture of the SOTAB-I software enabled distribution of responsibilities and enhanced the clarity of the program and its flexibility to changes. The program code optimization helped to reduce the processor usage. This contributed to the reduction in power consumption and prevented the processor from overheating inside the pressure cell. An acoustic communication data frame was established that enabled transmission of critical information to the user on the mother ship. A checksum verification method was used to secure the control of the robot through downlink, giving it an immunity against noise.

Water column regions and robot operating modes were explained. A pyramidal hierarchy was established to define each control program priority. This architecture

enabled the robot to avoid dangerous situations and interrupt the control program to automatically perform software emergency ascend when a problem is detected.

The control algorithm for depth control and heading control was explained. The basic idea and characteristics of PID depth control, depth control with time estimation, and progressive depth control were described. Some simulation examples were given to give illustrate how the depth control and heading control work.

Some experimental results were shown to demonstrate the performance of SOTAB-I's control program. The Toyama Bay experiments on November 2014 and March 2015 demonstrated the performance of the depth control using only the PID control algorithm. The depth control with time estimation algorithm was applied in the Toyama Bay experiment on June 2015. The depth control performance in this experiment was much better than observed in the previous experiments.

SOTAB-I was able to reach the target depth with very small overshoot. Even though the Toyama Bay experiment on September 2015 was interrupted by the UMS leakage incident, from the collected data, we can confirm that the early stages of the progressive depth control were working.

Path planning simulation of SOTAB-I was also introduced. It is used to simulate the trajectory of SOTAB-I during operation in X, Y, and Z axes under the effect of a water current. Combined with the underwater spilled oil or methane plume behavior simulation, the best route for SOTAB-I going through the spilled oil or methane plume can be predicted. The starting point where SOTAB-I should be deployed by the mother ship can also be obtained. From this simulation, we can know the best place for SOTAB-I deployment, which allows us to find the spilled oil or methane plume faster.

A calculation method of water current velocity using SOTAB-I was proposed. The data of water current profile is essential for the prediction of spilled oil behavior.

From the Gulf of Mexico experiments in the USA, the surveying abilities of SOTAB-I in shallow water were demonstrated. The water column distribution of dissolution of substances and water currents as well as the temperature and salinity were measured. The UMS could measure the variation in the concentration of various substances simultaneously, such as methane, oxygen, and carbon dioxide. In these experiments, a vertical water column survey was conducted within 50 m water depth.

From the Komatsushima experiment and first round experiment at Toyama Bay in Japan, the oceanographic surveying abilities of SOTAB-I were extended. Not only profiles of temperature, salinity, and density, but also water column current profiles were measured, and their accuracy was shown by comparing estimated water column current profiles using DVL and ADCP and USBL and DVL with measurements by the mother ships. In the second round experiment at Toyama Bay, these efforts were continued to extend the range up to 700 m water depth.

Water column current profiles were obtained in deep water. These collected data will help to determine the environmental changes due to accidents and boost the accuracy of oil-drift simulations, which contributes to the efforts to avoid further damage that can be caused by oil spill disasters. On the other hand, Chiba et al. (2015) analyzed the characteristics of the flow pattern in Toyama Bay by onboard

ADCP observations down to 84 m water depth, finding out the anticlockwise eddy at the inner part of Toyama Bay in summer. If we combine the onboard ADCP observation and the observation of water column current profile in deep water by SOTAB-I, more detailed structure of the flow pattern can be clarified.

Appendix

Tables 3.10, 3.11, 3.12, 3.13, 3.14, 3.15, 3.16, 3.17, 3.18, 3.19 and 3.20.

Table 3.10 Characteristics of one pack lithium-ion battery

Ref	Paco KV-100 Li-Ion battery pack
Electric charge	10.0 Ah
Voltage	14.4 V
Capacity	144 Wh
Weight	1.4 Kg

Table 3.11 Processing unit specification

Ref	Advantech PCI-104, PCM-3363
Processors	Intel atom N455 single core, 1.66 GHz, Cache 512 KB
	Intel atom D525 dual core, 1.8 GHz, Cache 1 MB
Memory	1GB DDR3 800 MHz
Interfaces	USB 2.0, RS-232, RS-422/485, SMBus (configurable to I2C), Ethernet, PS/2, GPIO
Power supply voltage	5 V
Power consumption	N455: typical 7.02 W/maximum 11.825 W
	D525: typical 9.25 W/maximum 13.475 W

Table 3.12 Thruster specification

Ref	Mitsui thruster model 260
Voltage	24 V
Nominal current	12A
Thrust force	35.28 N forward, 26.46 N backward
Maximum depth	2000 m
Weight	2 Kg

Table 3.13 Main characteristics of USBL system of SOTAB-I

Ref	LinkQuest Inc. TrackLink 5000HA
Accuracy	Positioning: 0.15°
	Slant range: 0.3 m
Working range	Up to 5000 m
Operating beam width	120°
Operating frequency	14.2–19.8 kHz
Maximum depth	Transponder up to 7000 m
	Transceiver up to 20 m
Power consumption	Transmit mode: 40 W
	Receiver mode: 1 W

Table 3.14 Main characteristics of GPS receiver of SOTAB-I

Ref	Garmin GPS 15 L
Update rate	1–900 s
Acquisition times	Reacquisition: less than 2 s
	Warm: approximately 15 s
	Cold: approximately 45 s
GPS accuracy:	Position: <15 m, 95 % typical
DGPS (WAAS) accuracy	Position: <3 m, 95 % typical

Table 3.15 Main characteristics of GPS compass on the ship

Ref	Hemisphere GPS compass VS101
Update rate standard	10 Hz; optional 20 Hz (position and heading)
Horizontal accuracy	<0.6 m 95 % confidence (DGPS1)
Heading accuracy	<0.15°rms at 1.0 m antenna separation
Pitch/roll accuracy	<1°rms
Typical acquisition times	Cold start <60 s, warm start <20 s, hot start <1 s
Power consumption	∼5 W nominal

Table 3.16 Main characteristics of the CTD sensor of SOTAB-I

Ref	CTD sensor SBE-49 FastCAT
Constructor	Sea-bird electronics
Sampling rate	16 samples/s
Range	Temperature: −5 to +35 °C
	Conductivity: 0–9 S/m
	Pressure: 0–7,000 m
Resolution	Temperature: 0.0001 °C
	Conductivity: 0.00005 S/m in oceanic waters
	Pressure: 0.002 % of full scale range
Weight	In air 2.7 kg, in water 1.4 kg

Table 3.17 Main characteristics of the ADCP/DVL of SOTAB-I

Ref	Navigator DVL WHN1200
Constructor	Teledyne RD instruments
Operating frequency	1200 kHz
Maximum depth	3000 m
Built-in sensors	Water temperature gauge, inclinometer, compass
Beam angle	30°
Water track velocity (ADCP)	Layer size selectable from 0.25 to 5 m
	Number of layers is selectable from 1 to 128
Bottom track velocity (DVL)	Altitude from four individual measurements
	Minimum altitude 0.5 m
	Maximum detectable altitude 30 m
	Velocity range: −/+10 m/s
	Long term accuracy: ±0.2 % ±0.1 cm/s

Table 3.18 UMS Specifications

Ref	SRI
Mass analyzer type	Linear quadrupole mass filter
Mass range	1–200 amu
Inlet system	Membrane introduction (PDMS)
Power consumption	60–80 W
Operation voltage	24 VDC
Maximum deployment time	10–14 days (exhaust limited)
Dimensions	Diameter 24 cm, length 64 cm
Weight	In air 35 kg, in water 5 kg neg.
Depth capability	2000 m

Table 3.19 Compass specifications

Ref	PNI's FieldForce TCM-XB
Accuracy	Heading 0.3°RMS
	Pitch 0.2°RMS
	Roll 0.2°RMS
Resolution	Heading <0.1°RMS
	Tilt <0.01°
Range	Heading: 0–360°
	Pitch: ±90°
	Roll: ±180°
Maximum sample rate	30 samples/s
Supply voltage	3.6–5 V
Calibration	Hard and soft iron

Table 3.20 IMU specification

Attitude and heading	
Range	Heading: roll:±180°
	Pitch: ±90°
Static accuracy	Heading: 2.0° RMS
	Pitch/roll:0.5° RMS
Angular resolution	<0.05°
Output rate	400 Hz
Gyro specifications	
Range:	±2000°/s
In-run bias stability:	<10°/h
Linearity	<0.1 % FS
Noise density	0.0035°/s $\sqrt{Hz}$
Bandwidth	256 Hz
Alignment error	±0.05°
Resolution	<0.02°/s
Accelerometer specifications	
Range	±16 g
In-run bias stability	<0.04 mg
Linearity	<0.5 °FS
Noise density	<0.14 mg/$\sqrt{Hz}$
Bandwidth	260 Hz
Alignment error	±0.05°
Resolution	<0.5 mg
Pressure sensor specifications	
Range	10–1200 mbar
Resolution	0.042 mbar
Accuracy	±1.5 mbar
Electrical	
Input voltage	4.5–5.5 V
Max power consumption	220 mW
Digital interface	Serial TTL, RS-232

References

An E, Dhanak MR, Shay LK, Smith S, Leer JV (2001) Coastal oceanography using a small AUV. J Atmos Ocean Technol 18:215–234

Azuma A, Nasu, KI (1977) The flight dynamics of an ocean space surveying vehicle. Institute of Space and Science, University of Tokyo, Tokyo, Japan. Report No. 547, Vol. 42, No. 2, pp 41–90

Bell RJ (2009) Development and deployment of an underwater mass spectrometer for quantitative measurements of dissolved gases. Ph.D. thesis, University of South Florida,St. Petersburg, Florida

Bell RJ et al (2007) Calibration of an in situ membrane inlet mass spectrometer for measurements of dissolved gases and volatile organics in seawater environ. Sci Technol 41:8123–8128

Bell RJ et al (2011) In situ determination of total dissolved inorganic carbon by underwater membrane introduction mass spectrometry. Limnol Oceanogr Methods 9:164–175. doi:10.4319/lom.2011.9.164

Chiba H et al (2015) The characteristics of the flow pattern in Toyama Bay by onboard ADCP observations -Anticlockwise eddy at the inner part of Toyama Bay in summer

Choyekh M et al (2014) Vertical water column survey in the gulf of mexico using autonomous underwater vehicle SOTAB-I. Mar Technol Soc J: Vol. 49, No. 3, 88–101

Eriksen CC et al (2001) Seaglider: a long-range autonomous underwater vehicle for oceanographic research. IEEE J Ocean Eng 26(4):424

Fofonoff N, Millard R (1983) Algorithms for computation of fundamental properties of seawater. UNESCO Tech Pap Mar Sci 44:1–53

Handa YP (1990) Effect of hydrostatic pressure and salinity on the stability of gas hydrates. J Phys Chem 94:2652–2657

Harvey J et al (2012) AUVs for ecological studies of marine plankton communities. Sea Technol 53(9):51

Hess JL, Smith AMO (1964) Calculation of non-lifting potential flow about three dimensional bodies. J Ship Res 8(2):22–44

Jakuba MV et al (2011) Toward automatic classification of chemical sensor data from autonomous underwater vehicles, intelligent robots and systems. In: IEEE/RSJ international conference on intelligent robots and systems, pp 4722–4727

Johansen Ø et al (2003) Deep spill–field study of a simulated oil and gas blowout in deep water. Spill Sci Technol Bull 8(5–6):433–443

Joye SB et al (2011) Magnitude and oxidation potential of hydrocarbon gases released from the BP oil well blowout. Nat Geosci 4:160–164

Kawahara S et al (2014) Numerical investigation on behavior of methane gas/hydrate seeping out from deep sea floor. In: The 24th ocean engineering symposium, OES24-050.

Kessler JD et al (2011) A persistent oxygen anomaly reveals the fate of spilled methane in the deep gulf of Mexico. Science 21 331(6015):312–315

Maxino TC, Koopman PJ (2009) The effectiveness of checksums for embedded control networks. IEEE Trans Dependable Secure Comput 6(1), pp 59–72

Medagoda L, Williams BS, Pizarro O, Jakuba VM (2011) Water column current profile aided localization combined with view-based SLAM for autonomous underwater vehicle navigation. In: IEEE International conference on robotics and automation, pp 3048–3055

Mitchell R et al (1999) Estimates of total hydrocarbon seepage into the Gulf of Mexico based on satellite remote sensing images. EOS Suppl 80:OS242

Roemmich D et al (2009) The argo program observing the global ocean with profiling floats. Oceanography 22(2):34–43. doi:10.5670/oceanog.2009.36

Servio P, Englezons P (2002) Measurement of dissolved methane in water in equilibrium with its hydrate. J Chem Eng Data 47:87–90

Shaffer G et al (2009) Long-term ocean oxygen depletion in response to carbon dioxide emissions from fossil fuels. Nat Geosci 2:p105–p109

Short RT et al (2006) Detection and quantification of chemical plumes using a portable underwater membrane introduction mass spectrometer. Trends Anal Chem 25(7):637–646

Solomon EA et al (2009) Considerable methane fluxes to the atmosphere from hydrocarbon seeps in the Gulf of Mexico. Nat Geosci 2:p561–p565

Stanway MJ (2010) Water profile navigation with an Acoustic Doppler current profiler. OCEANS 2010, Sydney. doi:10.1109/OCEANSSYD.2010.5603647

Vickery K (1998) Acoustic positioning systems. A practical overview of current systems. In: Proceedings of the 1998 workshop on autonomous underwater vehicles. Fort Lauderdale, FL, USA, pp 5–17

Vogel M et al (2001) Real-time deepwater current profiling system. Proc. OCEANS 2001 (MTS/IEEE) 1:269–274

Wenner PG et al (2004) Environmental chemical mapping using an underwater mass spectrometer. TrAC Trends Anal Chem 23:288–295. doi:10.1016/S0165-9936(04)00404-2

Yang DH, Xu WY (2007) Effects of salinity on methane gas hydrate system. Sci China Ser D Earth Sci 50(11):1733–1745, Springer

Zhang Y, Willcox JS (1997) Current velocity mapping using an AUV borne acoustic Doppler current profiler. In: Proceeding of the 10th International symposium on unmanned untethered submersible technology, Durham, pp 31–40